PHASE EVOLUTION, MICROSTRUCTURE AND WEAR BEHAVIOR OF $Al_{0.5}CoCrFeNi_2$ HIGH ENTROPY SUPERALLOY AND $Al/Al_{0.5}CoCrFeNi_2$ COMPOSITES PROCESSED USING SPARK PLASMA SINTERING

By

ABHISHEK TIKAR

Bachelor of Engineering in Metallurgical Engineering

College of Engineering Pune

Maharashtra, India

Submitted to the Faculty of the
Graduate College of the
Oklahoma State University
in partial fulfillment of
the requirements for
the Degree of
MASTER OF SCIENCE
May 2023

PHASE EVOLUTION, MICROSTRUCTURE AND WEAR BEHAVIOR OF $Al_{0.5}CoCrFeNi_2$ HIGH ENTROPY SUPERALLOY AND $Al/Al_{0.5}CoCrFeNi_2$ COMPOSITES PROCESSED USING SPARK PLASMA SINTERING

Thesis Approved:

Dr. Sandip Harimkar

Thesis Adviser

Dr. A. Kaan Kalkan

Dr. Ritesh Sachan

Dr. Ranji Vaidyanathan

ACKNOWLEDGEMENTS

My deepest and sincere gratitude to my advisor, Dr. Sandip P Harimkar, Professor and Interim Head & Albert H. Nelson, Jr. Chair, Mechanical and Aerospace Engineering. I cannot imagine this transitional journey without his guidance and push for excellence. From starting as a master's student to shifting to PhD track and back to master's track, he has always been supportive of my decisions and motivated me to stay focused on my research irrespective of the obstacles. Dr. Harimkar always ensured that I had a conducive environment for research and made all resources available in a timely manner so I can execute my experiments. I am grateful to have had an opportunity to work with him. A special thanks to Dr. Shih-Hsun (Bruce) Chen, Assistant Professor, Department of Mechanical Engineering, National Taiwan University of Science and Technology for providing us with the high entropy alloy powder to carry out my research.

I am also thankful to Dr. Ritesh Sachan and his student Ashish Gupta for carrying out the TEM analysis of my specimens and adding valuable data to my thesis. Dr. Arvind Agarwal and Dr. Tanaji Paul from Florida International University helped me to carry out nanoindetation test for my specimen which surely elevated the quality of my work. Thank you so much for agreeing to help me at short notice and providing me with excellent results.

A special thank you to Dr. A. Kaan Kalkan and Dr. Ranji Vaidyanathan for their consistent support throughout my studies at Oklahoma State University. They have always enlightened me with their knowledge and lightened my stress with casual discussions. I will always be grateful to have Dr. Harimkar, Dr. Sachan, Dr. Kalkan and Dr. Vaidyanathan as my committee members and guide me through my master's.

And last but not least, I would like to thank my family and friends who stuck by me through thick and thin. They have been my biggest support system throughout my time at Oklahoma State University. I feel blessed to have the support of my family through all the decisions I made. They always encouraged me to work harder to achieve my goals. My friends back home and here in Stillwater, I could have never imagined being in United States without you all being by side all time.

Oklahoma State University and the town of Stillwater have been my home since Fall 2019 and will always have my heart, for here is where I found the best in me. As I await new opportunities in life, no matter where I move on this globe, I will always be a cowboy at heart. Go Pokes!!!

Acknowledgements reflect the views of the author and are not endorsed by committee members or Oklahoma State University.

Name: ABHISHEK TIKAR

Date of Degree: MAY, 2023

Title of Study: PHASE EVOLUTION, MICROSTRUCTURE AND WEAR BEHAVIOR OF $Al_{0.5}CoCrFeNi_2$ HIGH ENTROPY SUPERALLOY AND $Al/Al_{0.5}CoCrFeNi_2$ COMPOSITES PROCESSED USING SPARK PLASMA SINTERING
Major Field: MECHANICAL AND AEROSPACE ENGINEERING

Abstract: High Entropy Superalloys (HESA), an extension of high entropy alloys, exhibit excellent high temperature properties with low density, making them a potential replacement for expensive and heavy superalloys and to be used as reinforcement in metal matrix composites. While multiple processing routes are available for high entropy alloys, spark plasma sintering is becoming increasingly popular due to its ability to fabricate alloy powder in a short period of time. Spark plasma sintering can also be used for processing metal matrix composites. This work reports the phase evolution and microstructural development of gas atomized $Al_{0.5}CoCrFeNi_2$ high entropy superalloy powder fabricated using spark plasma sintering and, the wear properties of the sintered specimen. It also discusses the interaction of $Al_{0.5}CoCrFeNi_2$ reinforcement particles in aluminum matrix and its effect on wear properties of the composite material. The $Al_{0.5}CoCrFeNi_2$ alloy powder and all the specimen sintered in the range of 800℃-1050℃ showed an extremely stable single phase FCC structure. Relative density of 99% was achieved at temperatures of 1000℃ and above. Porosity pinning effect played an important role in densification process and grain growth. In all the sintered specimen, a combination of adhesive, delamination, oxidation, and abrasive wear was observed, with the coefficient of friction values recorded in the range of 0.6-0.7. $Al/Al_{0.5}CoCrFeNi_2$ composites was sintered using spark plasma sintering with varying holding time – 10 min, 15 min, 20 min and 30 min. Specimen with holding time 15 min and above developed an interdiffusion (ID) layer at the interface of reinforcement and the matrix. The interdiffusion layer was rich in Al (60%-80%) as it diffuses inward into the HESA particle whereas Ni, Co, Cr and Fe diffuse outward into the Al matrix. Nanoindentation results showed a sudden increase in hardness in the ID layer region which is higher than that of the HESA particle the matrix. TEM images revealed the formation of Ni_3Al nanoprecipitates in the ID layer resulting in the observed increase in hardness. Formation of ID layer in the composites reduced the wear loss to almost half in comparison to pure aluminum.

TABLE OF CONTENTS

LIST OF TABLES

LIST OF FIGURES

Figure Page

CHAPTER I

INTRODUCTION

1.1 Metals and Alloys

Metals are elements capable of donating valence electrons and forming anions. Metals have been used by humans since 6000BC and they are generally characterized by their ability to conduct heat and electricity, luster and in some cases their strength. Metals like gold and silver are mainly used in jewelry and electronic components whereas iron, copper, nickel, etc. find application in structural designs. Historians predict that humas first started using alloys around 3000BC and today, they dominate every aspect of our lives. An alloy is a solid solution containing one (or two) principal elements with other metals or non-metals in minor quantity added to it. Some of the most known alloys include steel (Fe+C), Brass (Cu+Zn) and Bronze (Cu+Sn). As human development progressed, pure metals were deemed inadequate for direct use. Sparing some exceptions, most pure metals lacked strength, oxidation resistance and corrosion resistance required for structural application. The addition of alloying elements to pure metals allowed us to modify the properties of pure metal and overcome the shortcomings possessed by them. For example, pure iron lacks toughness, oxidation and corrosion resistance which can be overcome by addition of carbon to form steel, which has superior properties to iron and is more reliable for structural applications. The addition of Co, Cr, Ni, etc. as alloying elements to steel allows us to further enhance properties of iron as desired. Today steel, brass, bronze, aluminum alloys and superalloys are widely used in automotive, aerospace, marines, defense, medical, etc.

With increasing demands of industry and a push towards green energy, there was a need to develop more complex, light weight and sustainable alloys.

1.2 High Entropy Alloy

High Entropy Alloy (HEA) are alloys consisting of five or more principal elements in equiatomic or near equiatomic concentration. The concentration of each principal elements lies in the range of 5 at% and 35 at% [1]. Defying the traditional concepts of metallurgy, these alloys form a simple lattice structure such as FCC and BCC. High entropy alloys are characterized by four core effects [2]:

1. High Configurational Entropy: The presence of multiple principal elements in the solid solution leads to a surge in system entropy which results in stabilization of the HEA by reducing the overall total free energy of the system.

   $\Delta G = \Delta H - T\Delta S$ ……as $\Delta S\uparrow$ - $\Delta G\downarrow$ (1.1)

2. Severe Lattice Distortion: When atoms of different principal elements dissolve into the solid solution to form a simple crystal structure, the difference in the size of individual elemental atoms cause severe distortion in the final lattice structure of the HEA (Fig 1.1).

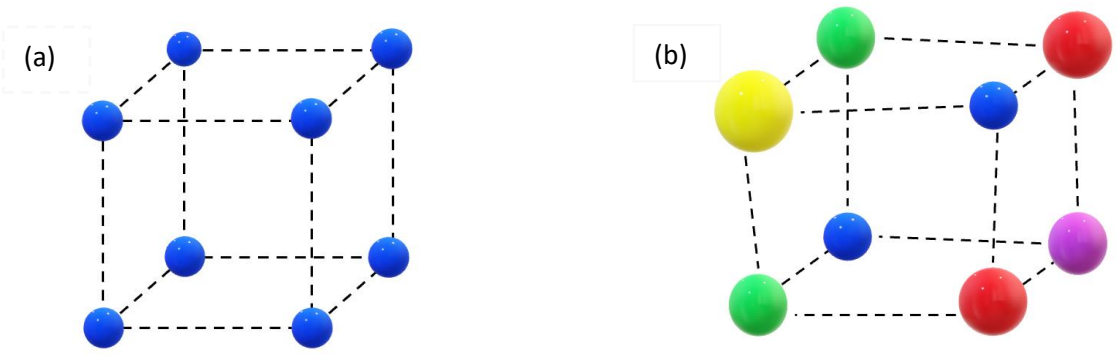

Fig 1.1. Representative images of crystal lattice structure for (a) conventional alloy, (b) high entropy alloy

3. Sluggish Diffusion: An atom diffusing through an HEA system, experiences changing atomic environment from point to point due to presence of multiple principal elements. This hinders the diffusion through high entropy alloys resulting in sluggish diffusion.
4. Cocktail Effect: The final set of properties owned by an HEA are a result of the constituent elements and their concentration.

Some of the most widely studied compositions of high entropy alloys were inspired by their conventional counterparts and mainly contain elements like Co, Cr, Fe, Mn, Ni, Cu, Al, etc. [3]. As mentioned earlier, HEAs form a simple crystal structure and studies have shown that it is possible to predict the final phase formation in these alloys. Valence Electron Configuration (VEC) can be used for predicting the phase formation and it can be calculated as follows [4]:

$$VEC = \sum_{i=1}^{n} c_i (VEC)_i \quad (1.2)$$

The relation between VEC and phase formation and stability are as follows:

VEC< 6.87 – Stable BCC phase

6.87 <VEC< 8 – Mixed FCC and BCC phases

VEC> 8 – Stable FCC phase.

High entropy alloys have showcased high thermal stability, excellent mechanical properties, good resistance to oxidation and corrosion compared to conventional alloys in varying environments and thus, have attracted attention of research community to study and develop these systems and explore possible applications.

Some of the recent developments in high entropy alloy have seen synthesis of new sub-groups of HEAs. These are-

Refractory High Entropy Alloys: These HEAs contain refractory elements like Mo, Nb, V, W, Ti, Zr, Hf, Ta, etc. as main constituent elements and are mainly targeted towards high temperature application [5,6].

Light Weight High Entropy Alloys: This subgroup of HEA aims at achieving superior mechanical properties at lower density values by using elements like Li, Mg, Al, Ti, etc. for synthesis [7–9].

Non-equiatomic High Entropy Alloys: These alloys do not follow the traditional HEA compositional definition and tend to have certain elements outside the concentration range of 5 at% and 35 at%. This is done to achieve application specific properties as per cocktail effect [10].

1.3 Composites

A composite material is made by combining two materials with different physical and chemical properties. The resultant composite has properties different from its parent component materials. A composite mainly consists of two entities- the matrix and the reinforcement. Matrix can either be polymer, metal or ceramic. Depending on the nature of matrix, reinforcement can be added to either increase the strength or the toughness of the material. Reinforcement be in the form of flakes, fibers, fillers, or particulates. Metal matric composites (MMC), especially with particulate reinforcement, are widely used in aerospace and automotive industries and for structural applications. High strength, good stiffness to weight ratio, resistance to high cycle fatigue, wear resistance, corrosion resistance, high thermal conductivity and low coefficient of thermal expansion give MMCs a leverage over conventional alloys and materials. Some of the most used metals used as matrix include iron, copper, nickel, titanium, and aluminum. The interaction and resultant bonding between the matrix and the reinforcement determines the properties of the composite material [11–18].

1.4 Processing Routes

1.4.1 Casting

Casting is a processing technique in which a metal is melted and poured into a mold for solidification. Alloys can be processed using this technique by melting the principal metal and adding the alloying elements to it and then solidifying it into a mold. Similarly, metal matrix composite can be processed by adding reinforcement particles into the molten matrix and mixing it for uniform distribution. Casting poses certain limitations like- defects which are unavoidable during the process; for processing alloys, the solid solution might need to be remelted multiple times which isn't energy efficient. Also, the surface finish of the final product is inferior.

1.4.2 Additive Manufacturing

Additive manufacturing involves deposition of layers of materials one over the other to create the desired 3D object. It is a very computer intensive processing technique. Various processes like direct metal deposition, selective laser melting, binder jetting, etc. fall under the category of additive manufacturing. Limitations such as cost of technology, limited choice of materials, slow speed of production and need for postproduction treatment have obstructed the use of this technology for mass production of bulk objects.

1.4.3 Powder Metallurgy

Powder metallurgy involves processing techniques which consolidate metallic powder without melting. Most commonly known powder processing technique is sintering. Metal, alloy, or metal matrix composite powder is compacted in desired shape under pressure and then placed in a furnace to form a compacted solid object. This process delivers products with excellent surface finish, gives greater control over the properties of the final product, produces less to no waste, and reduces energy consumption. Some limitations of this processing technology are- possibility

of uneven density distribution and resulting inferior mechanical properties, maintenance cost and cost of raw material. The metal powder required for sintering is primarily made by atomization process. Alloy powders can be synthesized either by atomization or mechanical alloying.

CHAPTER II

LITERATURE REVIEW

2.1 High Entropy Superalloy:

High Entropy Superalloy (HESA) is a new subgroup of high entropy alloys which are designed on the lines of conventional superalloys such as Ni-superalloys, Co-superalloys, Fe-superalloys, Cr-superalloys, etc. Conventional superalloys find a wide range of applications in fields like aerospace, marine, nuclear reactors, chemical processing, manufacturing gas turbines, heat exchangers, etc. This is possible because conventional superalloys exhibit excellent strength and creep resistance at high temperatures, excellent oxidation resistance and corrosion resistance. But the existing conventional superalloys have certain limitations. For example, conventional superalloys have very high density, Inconel 718 has a density of 8.2g/cc and Inconel 625 has a density of 8.4g/cc. Further, conventional superalloys contain certain heavy and expensive elements like Nb, Ta, W, V, Re, Ru, etc. which are responsible for boosting the mechanical strength of these alloys at higher operating temperatures. Additional problems like processing and machining of these conventional superalloys limit their application. Hence, high entropy superalloys were developed to overcome these limitations of conventional superalloys [19, 20].

The idea of high entropy superalloys aims to reduce the density and cost of superalloys by limiting or even eliminating the need of heavy elements and relying on the high entropy effect to provide stability and strength to the composition. As a result, we obtain a high entropy superalloy with properties comparable to that of conventional superalloys, lower density, higher stability, easy processing and at reduced cost. Several research groups have performed studies on processing, analyzing, and testing of these high entropy superalloys [21–23]. Yeh *et al.* designed and processed high entropy superalloys on the lines of Ni-superalloys by arc-melting [24]. The HESA was mainly composed of Ni, Co, Cr, Fe, Al, and Ti. Multiple specimens were made by varying the elemental concentration to conduct a comparative study. All specimens had a density below 8g/cc. The HESA had a stable FCC phase with γ' as secondary phase uniformly distributed throughout the material which was formed as a result of addition of Ti. The presence of secondary phase increased the strength of the HESA. The material also had the potential to have good oxidation resistance. It should be noted that superior mechanical properties were achieved in this HESA without the addition of heavy refractory elements which lowered the cost of production. Zhang *et al.* synthesized $Ni_{45-x}(FeCoCr)_{40}(AlTi)15Hf_x$ (x = 0, 0.2 at. %) high entropy superalloy [21]. From analysis, it was found that this HESA had a single-phase FCC structure with γ' nanoparticles precipitated throughout the alloy. The presence of these precipitates resulted in strengthening of the HESA. The tensile test data showed that at 750℃, the HESA has tensile strength comparable to Ni-superalloys. Chen *et al.* studied the effect of heat treatment on the microstructure and precipitation in high entropy superalloy consisting of Ni, Co, Cr, Fe, Al, Ti, Mo, W and Nb. It was found that γ' phase, as in earlier studies, precipitated in the HESA [25]. The heat treatment study revealed that the shape of precipitates can be changed by changing the heat treatment temperature which can be further used for achieving the desired mechanical properties in the material.

All the studies conducted so far on high entropy superalloys have chosen a composition which ultimately resulted in formation of γ' secondary phase. This secondary phase is then responsible for strengthening the alloy and therefore, focus has been conducted on the composition, stability, morphology, and mechanical aspect of this secondary phase. No literature is available on a single-phase high entropy superalloy without secondary phase. As a result, the understanding of high entropy effect in these alloys is not well understood. Lack of studies on single phase HESA compositions, their processing, stability, and properties greatly undermines the potential these materials have for structural applications. Adjusting the elemental concentration or composition, it is possible to synthesize a single-phase high entropy superalloy. If the high entropy superalloy maintains its phase stability and exhibits good mechanical properties, it can attract a wide range of applications like high temperature mechanical parts offering a tradeoff between strength and toughness and ease of machining. It can also be used as particulate reinforcement in metal matrix composites.

2.2 Aluminum/High Entropy Alloy Composites

Aluminum is one of the most widely used metal matrix in processing of composites. Aluminum matrix composites (AMC) are very light weight and exhibit a good balance of ductility and strength. Therefore, AMCs find applications not only in the field of aerospace and automotive but also defense, marine and medical [26–30]. Aluminum matrix composites are also very economical to process and produce considerably less carbon emission. Some of the most used particulate reinforcements in AMCs include SiC, TiC, Al_2O_3, WC, Fe_3O_4, ZrO_2, TiN, ZrN, WB, TiB_2, etc. The properties of MMCs depend on the wettability of the reinforcement particles and their bonding with the matrix phase. The incoherency of ceramic particles with aluminum results in weak bonding of the reinforcement with the matrix phase [31–33]. An alternative to ceramic reinforcement is metallic glass particles. But these metallic glass particles are susceptible to

crystallization at higher temperatures which can destabilize the interface between the matrix and reinforcement and increase the possibility of a fracture occurring in the material [34, 35].

The structural stability and excellent mechanical properties of HEAs made them a possible contender to be used reinforcement in the metallic matrix. Additionally, HEAs have greater coherency with metallic matrix because of which we can expect improved wettability and good bonding between them. Multiple studies have been conducted using different metal matrices which were reinforced with HEA particles [36–38], but a significant number of studies have focused on the testing just the possibility of using HEA particles as reinforcement in aluminum matrix [39–42]. Zhang *et al.* synthesized an AMC using $AlCoCrFeNi_2$ HEA particles as reinforcement using ultrasonic processing technology [43]. The processing of this composite led to precipitation of secondary phases at grain boundaries resulting in grain refinement. They were able to modulate the mechanical properties of the composite by identifying the optimum amount of reinforcement to be added. *Yuan et al.* processed another AMC using CoCrFeMnNi HEA particles as reinforcement using spark plasma sintering[44]. It was revealed that during sintering, the elements in HEA reacted with aluminum and copper, which was present in the matrix, to form secondary phases. The good wettability of HEA particles and formation of interdiffusion layer improved the hardness of the composite. The nanoindentation data for the same showed that interface acts as load transfer medium between the matrix and the reinforcement thus, strengthening the matrix. *Li et al.* processed an AMC with BCC phase $Al_{0.8}CoCrFeNi$ HEA particles as reinforcement, using friction stir processing [45]. They observed a significant improvement in mechanical properties of the matrix material thus upholding the idea of potentially using HEA as reinforcement in AMCs.

The understanding of interaction of aluminum matrix and HEA particle composition is still not well established, limiting the particle application of HEAs as reinforcement. Development of new aluminum matrix composites with high entropy alloy reinforcement has only focused on the

compatibility of the two materials due to their metallic nature and the strength of HEA reinforcement. This also included HEA reinforcement which underwent phase transformation during processing of composite. No study has been conducted so far highlighting interaction of aluminum matrix with an HEA which has similar crystallography and high stability over a wide range of processing temperatures. Analyzing an Al/HEA composite on the line of composition, crystallography, processing, and interface reaction is necessary. Developing this understanding will allow us to choose HEA compositions best suited for reinforcement purposes in aluminum matrix composites. If reinforcing aluminum matrix with single phase FCC high entropy superalloy results in better wetting and compatibility of the two materials, the high entropy super alloy can serve as an alternative to ceramics and metallic glass as reinforcement.

CHAPTER III

OBEJCTIVES AND METHEDOLOGY

The composition of high entropy superalloys studied so far mainly constitutes Al, Co, Cr, Fe and Ni. If we can eliminate the alloying elements such as Ti, Nb, Hf etc. we can eliminate the formation of γ' and other secondary or metastable phases. Therefore, by choosing an appropriate concentration of Al, Co, Cr, Fe, Ni, we can study a single-phase high entropy superalloy to understand the phases, microstructure, and mechanical properties of it.

3.1 Objectives

1. First objective is to investigate the phase stability, microstructure, and wear behavior of $Al_{0.5}CoCrFeNi_2$ HESA. This was carried out by sintering the specimen using spark plasma sintering at varying processing temperatures.

2. Second objective is to investigate the interaction between aluminum and $Al_{0.5}CoCrFeNi_2$ high entropy superalloy particles as a result of spark plasma sintering to determine their compatibility to develop a composite material. The interaction between $Al/Al_{0.5}CoCrFeNi_2$ also affects the wear behavior of the composites and was hence investigated here as well.

3.2 Material Selection

$Al_{0.5}CoCrFeNi_2$ high entropy superalloy (HESA) will be used for studying a single-phase high entropy superalloy and the effect of processing parameters on its phase stability, microstructure, and mechanical properties. The HESA powder for this work was provided by Dr. Shih-Hsun (Bruce) Chen, Assistant Professor, Department of Mechanical Engineering, National Taiwan University of Science and Technology The scanning electron microscopy (SEM) image of HESA particles is shown in Fig 3.1. The size of these particles range between 10µm-60µm.

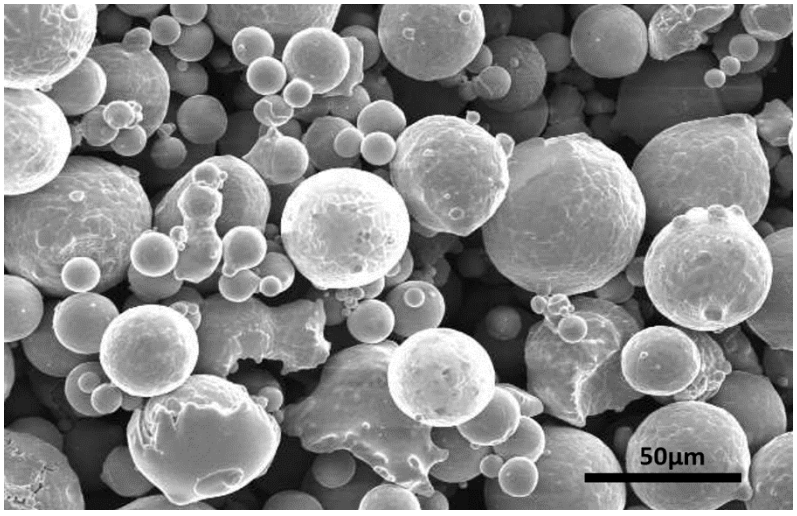

Fig 3.1. SEM image of $Al_{0.5}CoCrFeNi_2$ high entropy superalloy used for study.

The composition of $Al_{0.5}CoCrFeNi_2$ high entropy superalloy acquired using electron dispersive spectroscopy (ESD) is given in Table 3.1.

Element	Al	Co	Cr	Fe	Ni
Concentration (at%)	9	17.66	17.66	17.66	38

Table 3.1. Composition of $Al_{0.5}CoCrFeNi_2$ high entropy superalloy acquired using EDS.

Unlike the high entropy superalloys studied so far, $Al_{0.5}CoCrFeNi_2$ does not contain any traces of refractory elements or Ti, which are mainly responsible for formation of secondary phases. And the valence electron configuration (VEC) calculated for this high entropy superalloy is 8.14

hence, we may expect it to be the first single phase FCC high entropy superalloy developed so far without γ' or any other secondary phases. The compositional proximity of this HESA to Ni-superalloys without added refractory elements hint towards its high corrosion and oxidation resistance, increased toughness and reduced tensile strength. Hence, $Al_{0.5}CoCrFeNi_2$ can be considered for various future applications.

To understand the phase change and thermal stability of the high entropy alloy, differential scanning calorimetry (DSC) was performed with a heating rate of 10℃/min up to 1400℃. The DSC curve obtained in Fig 3.2 shows no sharp endothermic or exothermic peak, but we do observe structural relaxation occurring between 600℃ and 900℃.

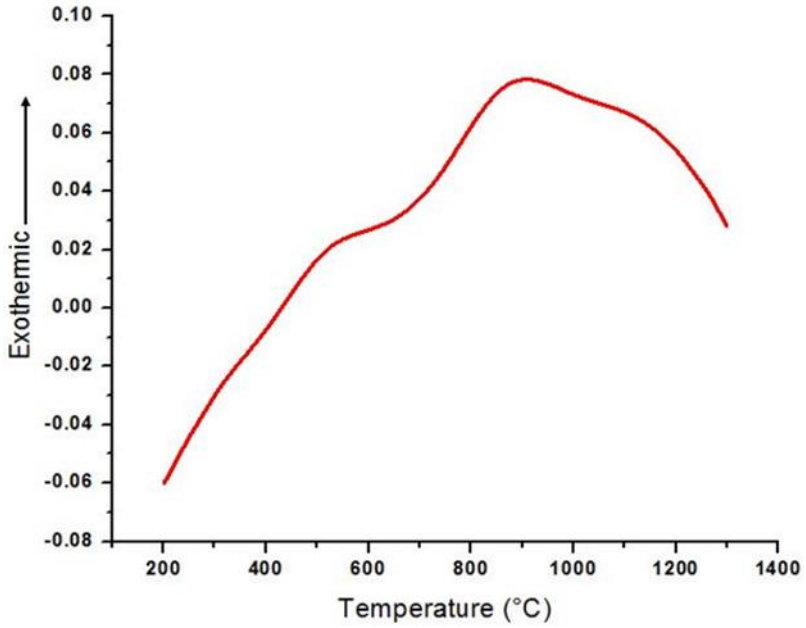

Fig 3.2. DSC curve of $Al_{0.5}CoCrFeNi_2$ high entropy superalloy.

For processing of $Al/Al_{0.5}CoCrFeNi_2$ composites, we choose pure aluminum matrix to avoid interaction with any species of alloying elements in aluminum. Hence, we will have a better understanding of the compatibility of the aluminum matrix and the HESA reinforcement.

3.3 Process Selection

Spark plasma sintering (SPS) is an advanced manufacturing technique which falls in the domain of powder metallurgy. This sintering technique utilizes uniaxial pressure and pulsed direct current to consolidate conducting powder in short fractions on time. Traditional hot pressing utilizes

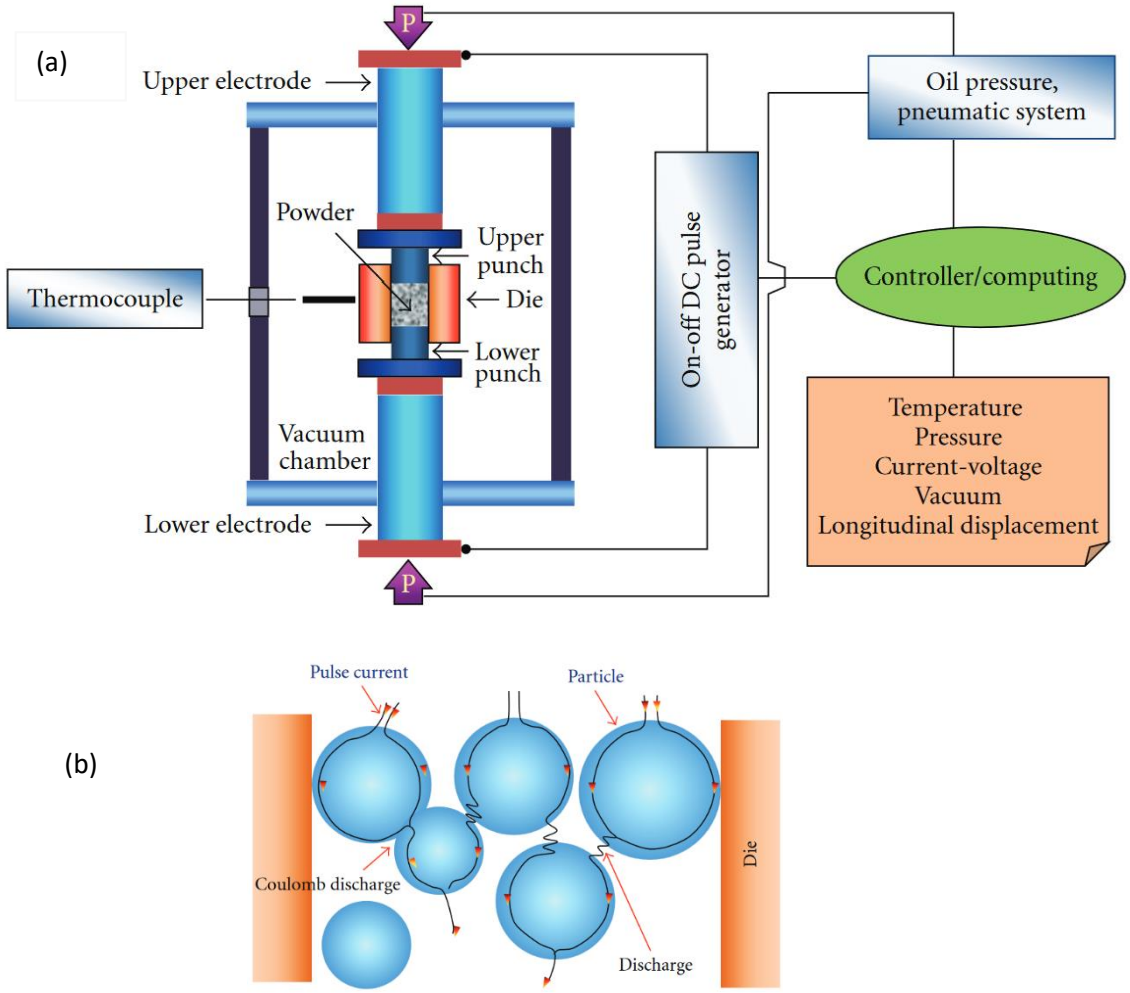

external heat source to promote diffusion and consolidation whereas Spark plasma sintering relies on the Joules Law of heating for fabrication of powder metal.

Fig 3.3. (a) Schematic of SPS process, (b) DC pulse current flow through the particles [46].

Some advantages of SPS over conventional sintering include fast heating and consolidation rate, high densification at lower temperature in less time, controlled atmosphere and greater control

over the entire process [47–49]. SPS gives us the ability to actively control the pressure, temperature, heating rate and atmosphere allows us to design complex processing cycles to achieve the densification and microstructure, and in certain cases, suppress the formation of metastable phases during processing. Study conducted by Zhang *et al*. on the densification of AlCoCrFeNi high entropy alloy showed SPS as a promising technique for rapid densification of alloy powder[50]. Similar conclusions were derived from the studies conducted by Joo *et al*. and Pohan *et al*. for varying elemental compositions of high entropy alloys [51, 52].

Therefore, choosing spark plasma sintering for processing of $Al_{0.5}CoCrFeNi_2$ high entropy superalloy and $Al/Al_{0.5}CoCrFeNi_2$ will allow us to fabricate specimens without developing unintended defects or phase transformations and help better understand the densification, phase evolution, microstructure, and resultant mechanical properties.

3.4 Experimental Methodology

3.4.1 Spark Plasma Sintering of $Al_{0.5}CoCrFeNi_2$, Analysis and Wear Test

Spark Plasma Sintering: Gas-atomized $Al_{0.5}CoCrFeNi_2$ High Entropy Super Alloy powder was used for this study. The powder particles had size ranging 10-60μm. The specimens were consolidated using Thermal Technology 10-3 Spark Plasma Sintering machine at 800℃, 850℃, 900℃, 950℃, 1000℃ and 1050℃ respectively for 15 min at a constant pressure of 50 MPa and heating rate of 100℃/min. The sintered specimens had a cylindrical shape with a diameter of 10mm and heigh ~2mm.

Analysis Technique: XRD analysis of the powder and the sintered specimens was performed using Philips X-Ray Diffractometer. The thermal analysis was carried out using Netzsch STA 449 F1 Jupiter. The theoretical density for the HEA was calculated using the rule of mixtures. Experimentally, the density of sintered specimens was determined using Archimedes principle. The specimens were analyzed using FEI Quonta 600F scanning electron microscopy. Optical microscope was used to analyze the grains in the microstructure. The hardness of the consolidated

specimens was measured using Clark CM- 700AT with a load of 3N. The hardness values reported here is an average of five or more measured values.

Wear Test: Ball on disk wear test was carried out with Nanovea Tribometer using 6mm aluminum oxide ball. The test was carried out for 1hr with 75rpm and load of 15N. The wear track was subjected to SEM- EDS analysis.

3.4.2 Spark Plasma Sintering of Al/$Al_{0.5}$CoCrFeNi$_2$, Analysis and Wear Test

Spark Plasma Sintering: Pure aluminum powder was mixed with 5 vol% of $Al_{0.5}CoCrFeNi_2$ high entropy superalloy powder using low energy ball milling for 1.5hrs. The powder mixture was then transferred into a graphite mold and sintered using spark plasma sintering. Sintering was performed at 525℃ and 70MPa with a heating rate of 100℃/min. Varying holding times – 10 min, 15 min, 20 min and 30 min were used during sintering. Disc shaped composite specimens with 10mm diameter and a thickness of approximately 3mm were mounted and polished to achieve a mirror finish.

Analysis Technique: The polished surface was further analyzed using optical microscopy, X-ray diffraction, SEM and EDS. To perform nanoindentation, specimen sintered for 20 min was polished again to acquire a clean oxide free surface. A load of 800μN was utilized to acquire data from the HESA particle, interdiffusion layer and matrix region using Nanoindentation. For TEM analysis, the specimen with 30 min holding time was cut into a small section of 2mm x 3mm, polished to reduce the thickness and exposed to ion beam.

Wear Test: The ball on disk wear test was carried out using a 6mm Silicon Nitride for 90 min at a speed of 100RPM and a load of 10N. The volume loss was recorded to calculate using nanovea profilometer and the wear track was further analyzed using SEM and EDS.

CHAPTER IV

RESULTS AND DISCUSSION

4.1 Analyzing the Phase Evolution, Microstructure and Wear Response of Spark Plasma Sintered $Al_{0.5}CoCrFeNi_2$ High Entropy Superalloy.

4.1.1 Phase Analysis

Previously conducted studies on spark plasma sintering of HEAs have shown that phase transformation may occur during densification, altering the microstructure and mechanical properties of the final product. Hence, the phases present in the starting $Al_{0.5}CoCrFeNi_2$ HESA powder and the specimens which were spark plasma sintered at different temperatures (800℃-1050℃) were analyzed using XRD in Fig 4.1 to identify any possible phase transformation. For the HESA powder and all the sintered specimens (111), (200) and (220) peaks were identified which indicates the presence of an extremely stable FCC phase, which also agrees with valence electron configuration rule for phase prediction. Unlike conventional superalloys and previously studied high entropy super alloys, no secondary phases were detected from the XRD spectra for $Al_{0.5}CoCrFeNi_2$.

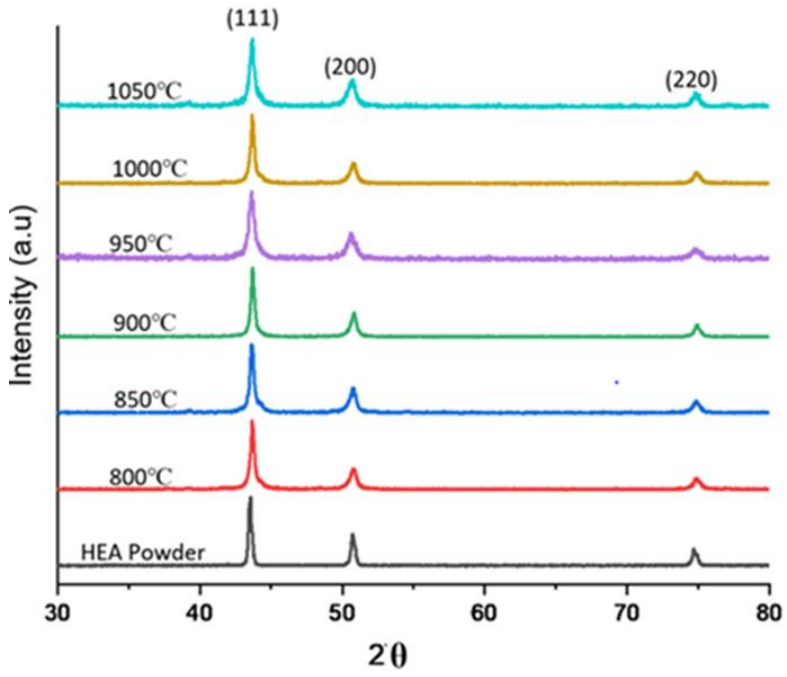

Fig 4.1. XRD pattern for Al0.5CoCrFeNi2 HEA powder and sintered specimen

In the study conducted by Wang *et al*. to understand the effect of addition of aluminum on the microstructure and the mechanical properties of $Al_xCoCrFeNi$ high entropy alloy, it was found that when aluminum concentration is less than 11 at%, a stable FCC is obtained [53]. Also, studies conducted by Tung *et al*., Sistla *et al*. and Liang *et al*. observed that nickel, with increasing concentration, tends to stabilize FCC phase in the microstructure [54–56]. $Al_{0.5}CoCrFeNi_2$ contains around 10 at% Al and 35 at% Ni and thus, it can be said that the stable FCC phase in the high entropy super alloy is a direct consequence of low concentration of Al and high concentration of Ni. Further, comparing the high entropy alloy XRD spectra with the constituent elemental XRD spectra, it is observed that only the peaks of Ni are retained. Therefore, it can be inferred that Al, Co, Cr, Fe dissolve in the Ni lattice causing severe lattice distortion and inducing

high entropy effect in the alloy. Hence, the high entropy alloy can be processed over a wide range of temperature maintaining a stable FCC phase.

4.1.2 Densification and Microstructural Analysis

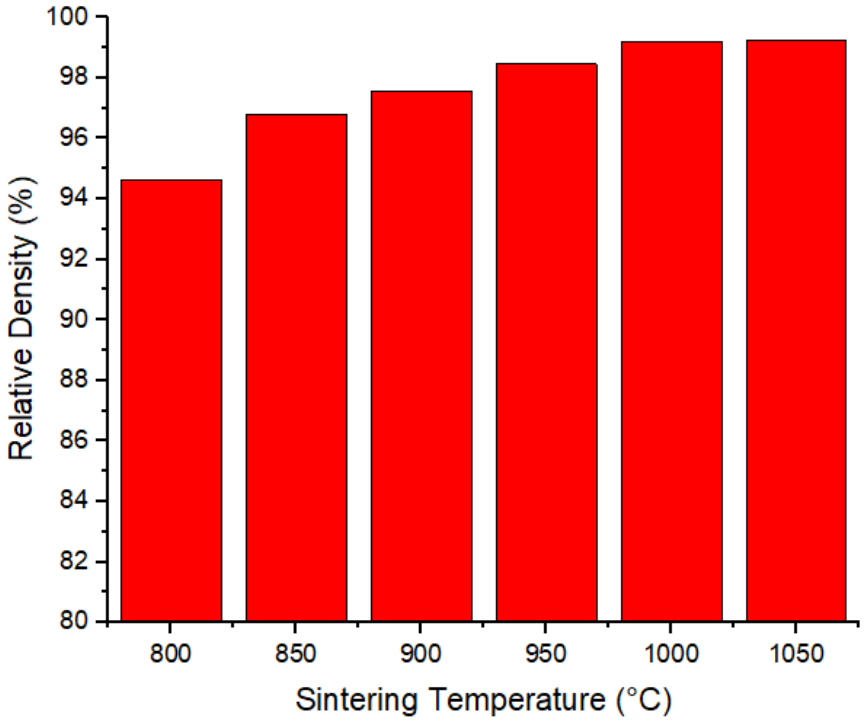

Fig 4.2. Relative density of sintered specimens with respect to sintering temperature.

The theoretically calculated value of density for $Al_{0.5}CoCrFeNi_2$ is 7.81 g/cc. This density value of $Al_{0.5}CoCrFeNi_2$ makes the alloy lighter than most superalloys which have a reported density greater than 8g/cc. The relative density results for all the sintered specimens are given in Fig 4.2. The lowest relative density, 94%, is recorded for specimen sintered at 800℃. The relative density increases with increase in sintering temperature and more than 99% relative density is recorded for specimen sintered at 1000℃ and 1050℃. Previous densification studies show that the following stages occur during spark plasma sintering- mechanical movement of powder particles, rearrangement with some degree of plastic deformation and neck formation due to joule heating. The alloy powder required for sintering can be produced either my mechanical alloying or

atomization route. During mechanical alloying, large powder particles are continuously fractured and welded, resulting into formation of a solid solution with metastable phases, extremely fine particles size (<5μm) and no well-defined shape[57]. Mechanical alloying has certain drawbacks like susceptibility to oxidation, inclusion of impurities and inhomogeneity[58]. On other hand, atomized alloy particles are produced from molten solution of elements in a controlled atmosphere to yield well defined spherical particles with high purity and homogeneity[59], [60]. As sintering is dependent on the contact area of powder particles, the shape of the particle and resultant available contact area tends to dominate the densification behavior. For mechanically alloyed powders with fine sized particles and no well-defined shape, on application of pressure during sintering, these particles rearrange themselves to minimize the porosity and maximize the contact surface. Thus, time required for necking is less and this results in quick densification of mechanically alloyed powder during sintering. In contrast, atomized powder particles which are generally bigger in size compared to mechanically alloyed powder particles and have a spherical shape, result in larger porosities and extremely small contact area during the initial stage of sintering. Although necking takes place at the contact surfaces, larger porosities exert Zener drag on motion of grain boundaries which makes it difficult to achieve complete densification. This phenomenon is known as pinning of grain boundaries by porosities, and it is largely observed during sintering of gas atomized particles[61]. To overcome the pinning effect, spheroidization of porosities is necessary which is possible by surface diffusion[62], [63]. As diffusion is a temperature dependent process, increasing sintering temperature can accelerate the surface diffusion rate and cause porosities to spheroidize[64].

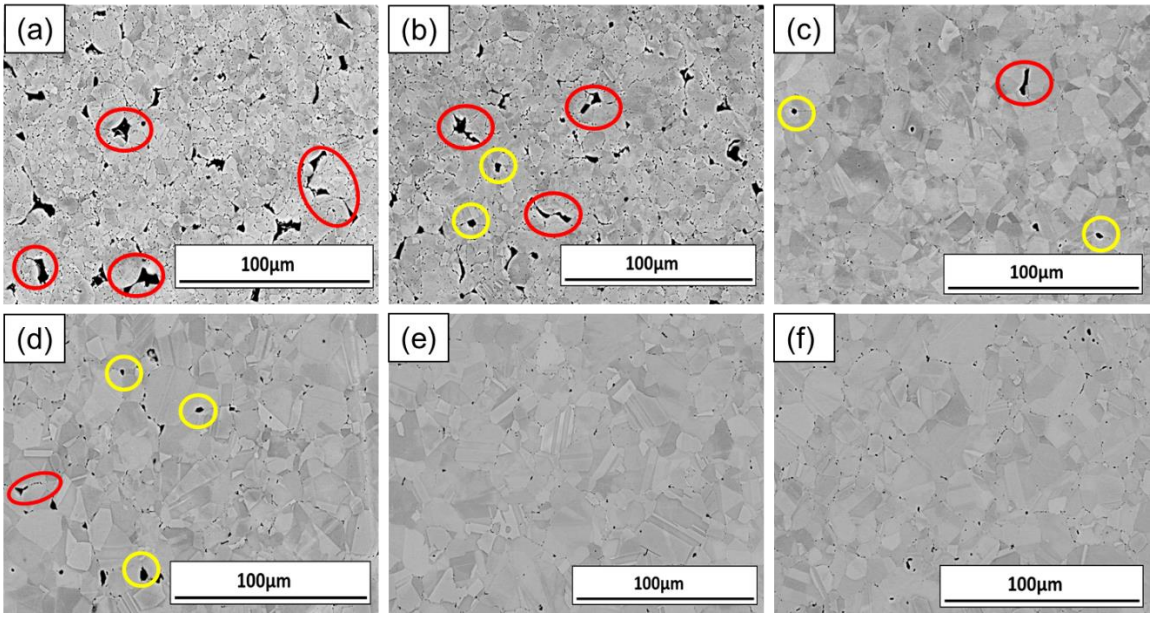

Fig 4.3. SEM images of single phase $Al_{0.5}CoCrFeNi_2$ for all sintered specimen: a) 800℃, b) 850℃, c) 900℃, d) 950℃, e) 1000℃ & f) 1050℃. The 'red' circles show porosities exerting Zener drag and 'yellow' circles show porosities after spheroidization.

This densification behavior of atomized alloy powder involving spheroidization of porosities can be observed in the microstructure of $Al_{0.5}CoCrFeNi_2$ sintered specimen. The microstructure of all the specimen sintered at different temperatures (800℃- 1050℃) are given in Fig 4.3. It can be observed that all the sintered specimens have a single-phase polycrystalline microstructure. At lower sintering temperature (800℃ & 850℃) the particle shape is retained in the microstructure and necking is observed at the contact surfaces. Large porosities are observed to distributed throughout the microstructure indicating that higher sintering temperatures must be utilized for complete densification. As the sintering temperature increases, the surface diffusion causes the porosities to spheroidize and achieve greater densification. It was observed that larger porosities required higher sintering temperatures for spheroidization. This spheroidizing of porosities with

increasing sintering temperatures is highlighted in Fig 4.3. Even with relative density greater than 99% for specimens sintered at 1000℃ and 1050℃, fine porosities can be observed dispersed

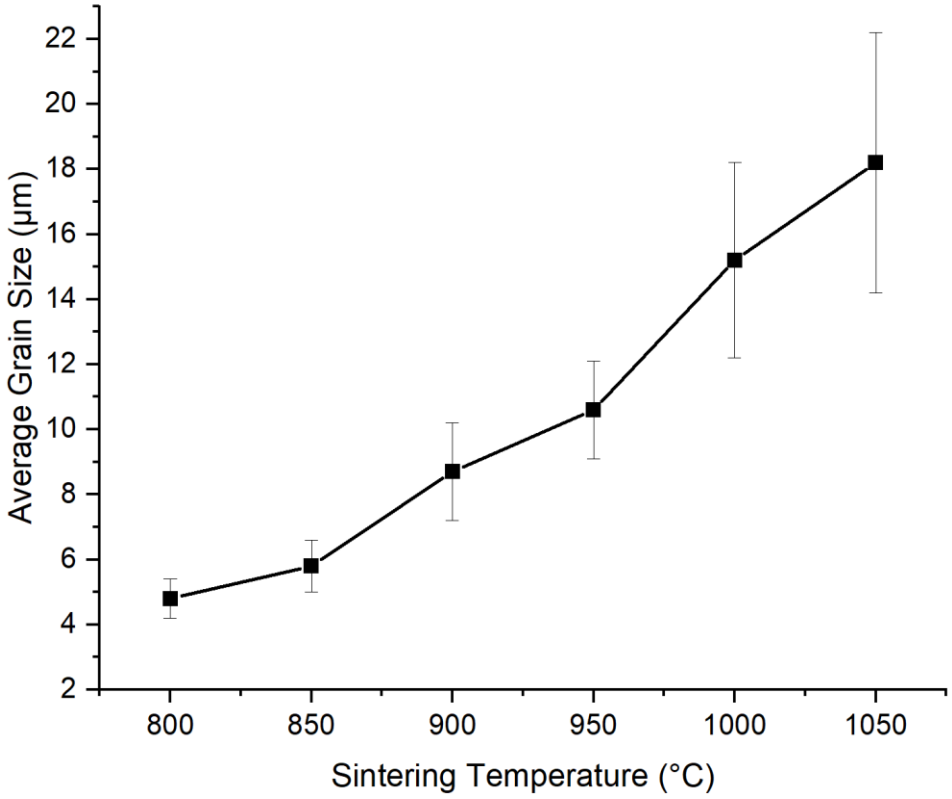

throughout the microstructure. As the pinning effect by porosities is overcome, an accelerated grain growth occurs in the sintered specimen.

Fig 4.4. Average grain size as a function of sintering temperature.

In Fig 4.4 we can observe that average grain size increases with increase in sintering temperature. But, as mentioned previously, grain growth is controlled by porosity pinning effect which in turn depends on the size of the porosity. Smaller porosities can be easily spheroidized resulting in grain growth at earlier stages compared to larger porosities that exert greater Zener drag and require higher temperature for spheroidization[65]. Thus, with average grain size data, it is equally important to analyze the grain size distribution in all the sintered specimens. Analyzing grain size distribution in the specimens, we observe that with increase in sintering temperature, a

broader variation in the grain size is visible. Therefore, standard deviation of grain size was calculated to better understand the grain size distribution in the sintered specimens. The standard deviation in the grain size for 800℃ sintered specimens was found to be 0.6µm which indicated equiaxed grain size distribution throughout the microstructure. The standard deviation increased with increase in sintering temperature and was found be around 4µm for specimen sintered at 1050℃. Certain abnormally large grains were also observed in specimen sintered at 1000℃ and 1050℃. This shows that the densification of $Al_{0.5}CoCrFeNi_2$ is controlled by powder particle size, shape, and misfit. The porosities resulting from the particle misfit inhibit the grain growth and densification.

4.1.3 Microhardness of Sintered Specimen

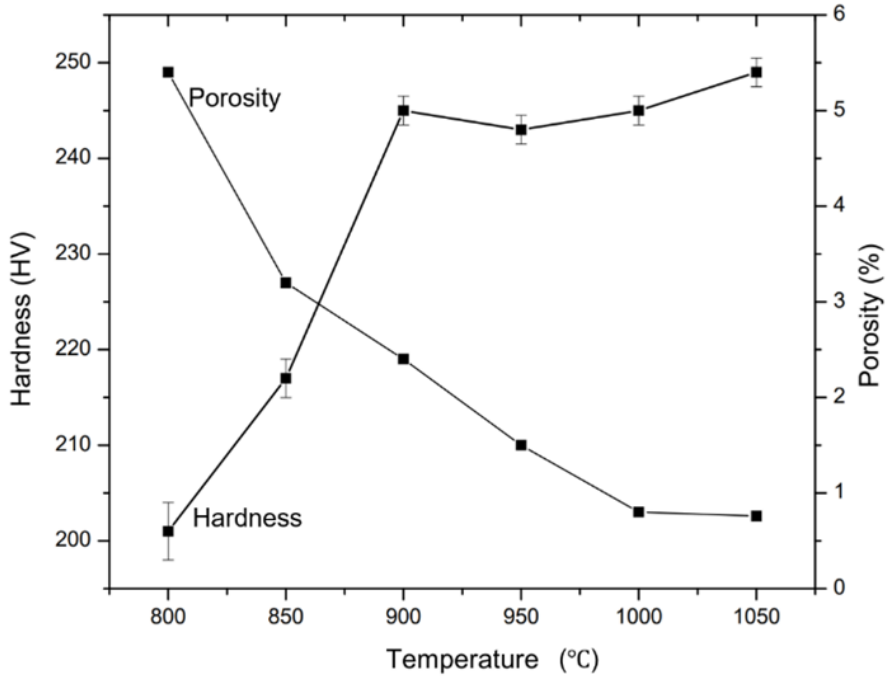

Fig 4.5. Microhardness & porosity of sintered specimens as function of sintering temperature.

Microhardness results are shown in Fig 4.5. It can be observed that hardness increases with increase in temperature. Low hardness values are recorded for specimen sintered at 800℃ and 850℃. The hardness of specimen sintered at 800℃ was recorded to be

201±10 HV whereas the specimen sintered at 850℃ had a hardness of 217±8 HV. The hardness value for specimens sintered at 900C, 950C, 1000C and 1050C did not show much variation with an average hardness value of 245±5 HV. This variation in hardness is the result of porosity[66]. Porosity acts as stress raisers and are the region of crack initiation. When the indentation applies force in a porous region, cracks develop, allowing the indent to go deeper and give lower values of hardness.

As a result of high percentage of porosity, specimens sintered at 800℃ and 850℃ have lower value of hardness. As specimens sintered from 900℃-1050℃ have low percentage porosity, the porosities do not interact with the indentation and do not affect the hardness results. Further, using ASTM E140, we can estimate the tensile strength of the material using hardness values. For $Al_{0.5}CoCrFeNi_2$, considering hardness value of 245±5 HV, tensile strength of the HEA can be estimated to be 790 MPa.

4.1.4 Wear Analysis

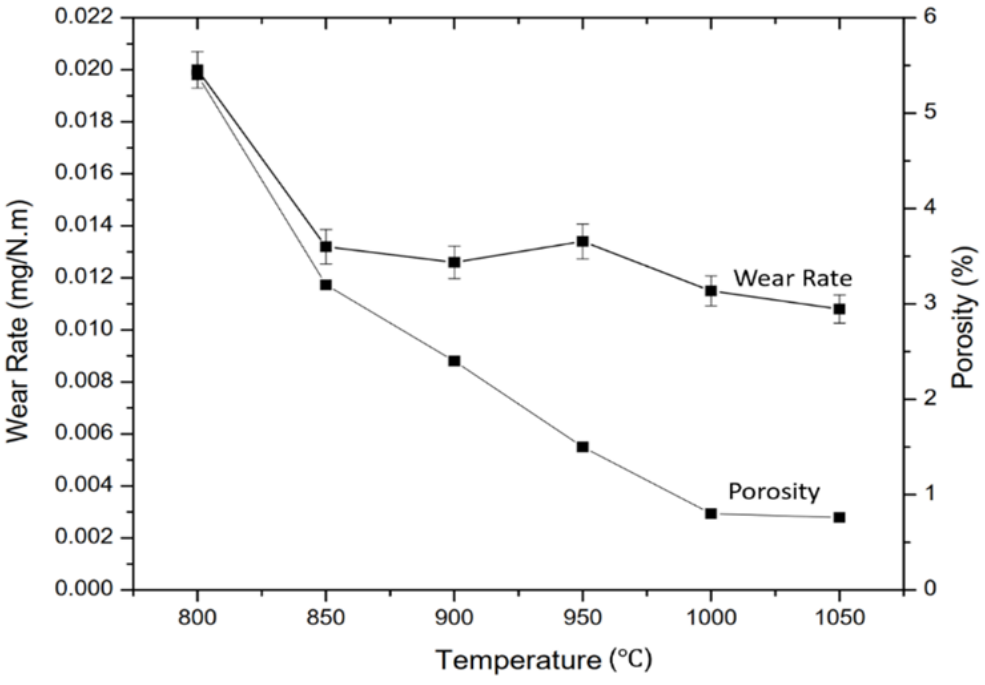

Fig 4.6. Wear rate and percentage porosity in sintered specimens as function of sintering temperature.

The wear rate and percentage porosity in the high entropy superalloy as a function of sintering temperature are shown in Fig 4.6. The highest wear rate is observed in specimen sintered at 800℃. Specimen sintered at 800℃ has highest percentage of porosity (~6%) with larger pore size. The alumina ball sliding over the surface develops multiple cracks originating from the porosity, resulting into greater wear mass loss. For specimens sintered from 800℃ to 1050℃, it is observed that wear rate decreases with decrease in percentage porosity in the sintered specimens. It should be noted that decrease in wear rate is not as significant as decrease in percentage porosity.

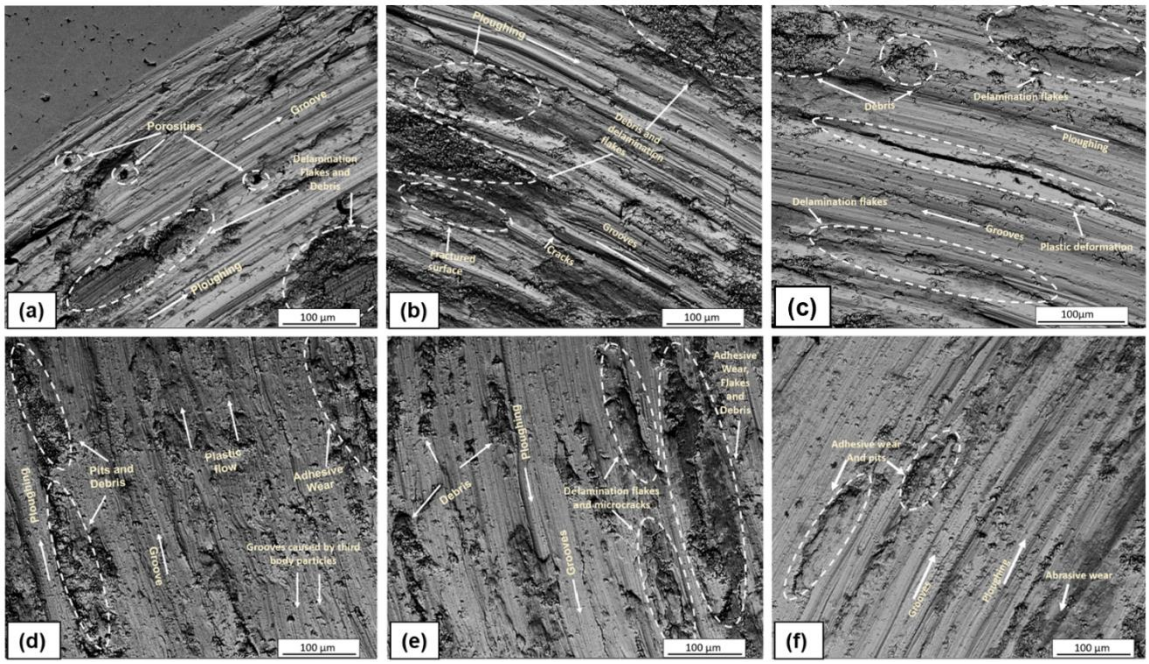

Fig 4.7. SEM images of wear track for specimens sintered at a) 800℃, b) 850℃, c) 900℃, d) 950℃, e) 1000℃, f) 1050℃.

The SEM analysis of wear tracks in Fig 4.7 show presence of grooves, scratches and signs of material being ploughed out from the region. The depth of the ploughed region and the grooves appears to be decreasing with increase in specimen density as reduced porosity inhibits the formation of cracks and their growth. Large porosities are clearly visible in the wear track for specimen sintered at 800°C. Delamination and microcracks are observed in the wear track of each specimen. The intensity of plastic deformation in the wear track region reduces with increase in specimen density. Pits and material removal caused by adhesive wear and fine grooves caused by third body friction are also seen in all the wear tracks. Minor signs of abrasive wear are also seen in the specimens. Thus, from the analysis of SEM data for the wear tracks, we can state that it is

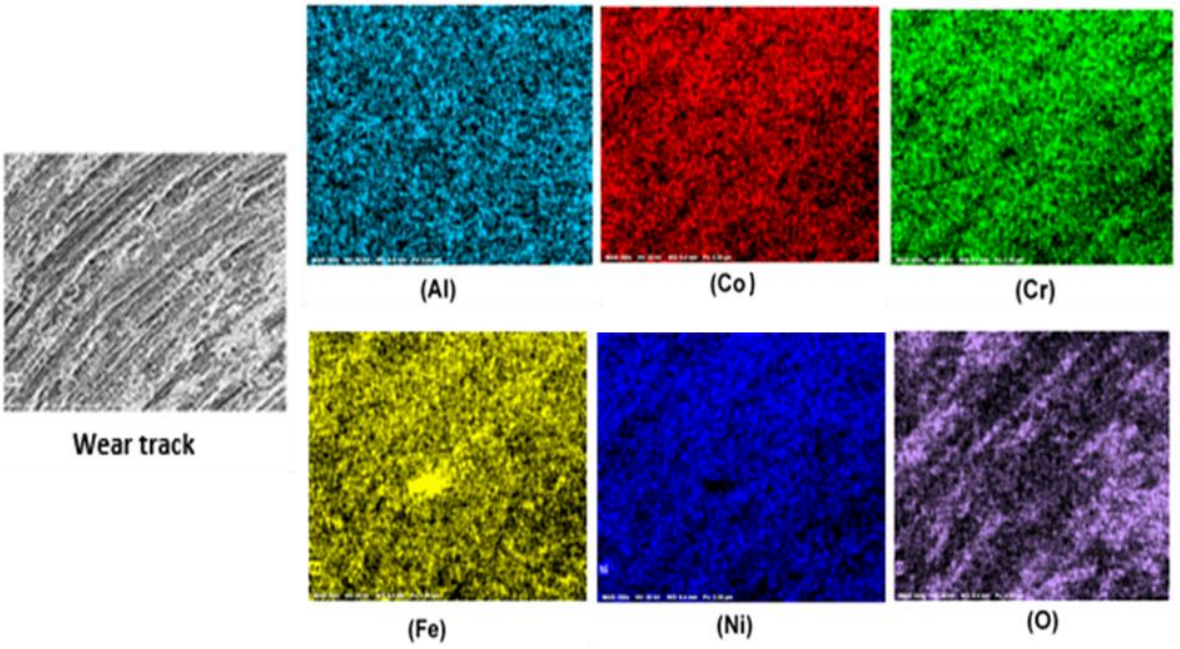

combination of adhesive wear, delamination, and abrasive wear. Unlike Ni-superalloys, absence of precipitates makes it easy for the HESA material to plastically deform and fracture off the specimen.

Fig 4.8. EDS mapping of the wear track for specimen sintered at 1000°C.

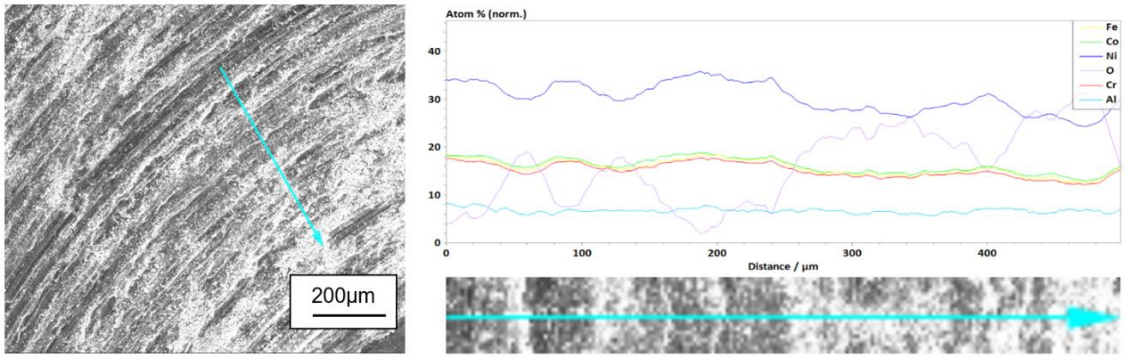

Fig 4.9 : EDS line scan of wear track for specimen sintered at 1000℃

Elemental Composition of Wear Track						
Specimen	Al (at%)	Co (at%)	Cr (at%)	Fe (at%)	Ni (at%)	O (at%)
800℃	7.60	14.58	13.84	14.32	27.56	22.07
850℃	6.33	15.17	13.96	14.47	28.54	21.52
900℃	5.88	13.94	13.06	13.35	26.19	27.55
950℃	5.93	14.52	13.71	14.16	27.45	24.21
1000℃	6.63	15.89	14.93	15.45	30.02	17.07
1050℃	6.12	15.29	14.55	14.83	28.81	20.38

Table 4.1: EDS line scan results for wear tracks in the sintered specimen.

To further understand the wear mechanism, EDS analysis was performed on the wear tracks of the sintered specimen. The EDS mapping and EDS line scan showed the presence of high concentration of oxygen in the wear track region. Fig 4.8 and 4.9 show the EDS mapping and line scan results of wear track for specimen sintered at 1000℃ respectively. Oxygen concentration as high as 30 at% was recorded in certain regions where debris are located whereas the wear surface has oxygen concentration of around 10%. Similar results are obtained for all other specimens. Table 4.1 shows concentration of different elements in the wear track region obtained from EDS analysis. Under dry

sliding conditions, high local temperatures are attained in the specimen which allows the formation of an oxide film. This film subsequently breaks to form the wear debris which act as third body particles [67]. Hence, from the EDS analysis it can be said that oxidation wear assisted with adhesive, delamination, and abrasive wear shape the wear behavior of the high entropy super alloy. The porosities also produce fluctuation in the instantaneous values of coefficient of friction (COF) in the initial stage of wear. As the wear debris occupy these porosities in the specimen, COF starts to stabilize. The COF stabilizes quicker in the specimens with less porosity. The coefficient of friction for $Al_{0.5}CoCrFeNi_2$ was found to be in the range of 0.6-0.7.

4.2 Interdiffusion Layer Formation and its Effect on Wear Properties of Al/$Al_{0.5}CoCrFeNi_2$ High Entropy Superalloy Composites.

4.2.1 $Al_{0.5}CoCrFeNi_2$ High Entropy Superalloy Distribution in Al Matrix

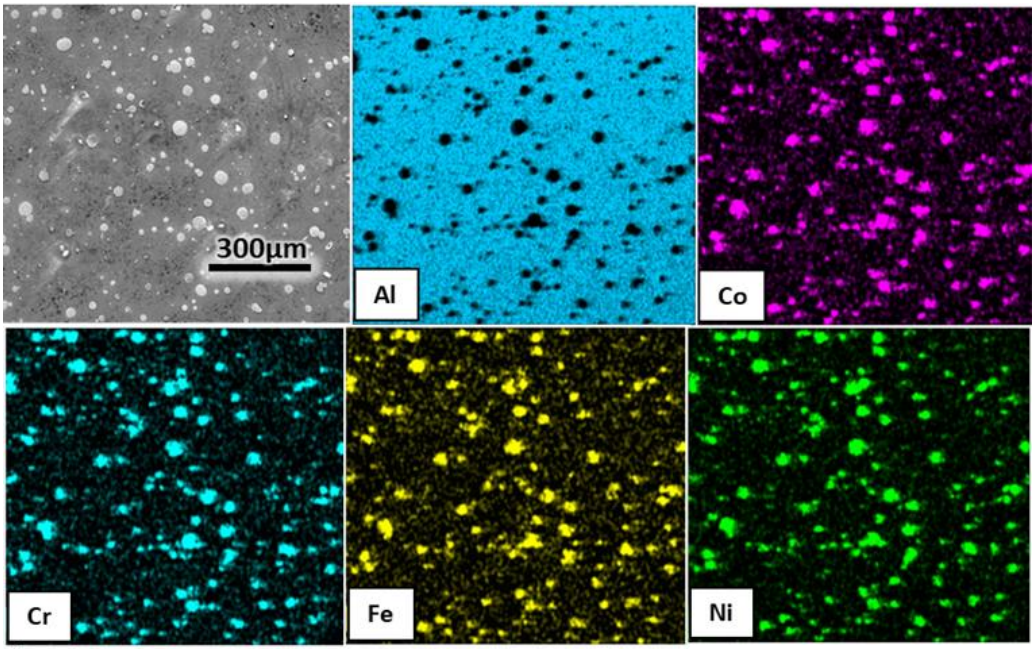

Fig 4.10. SEM image of 10min sintered composite specimen and EDS mapping of the same

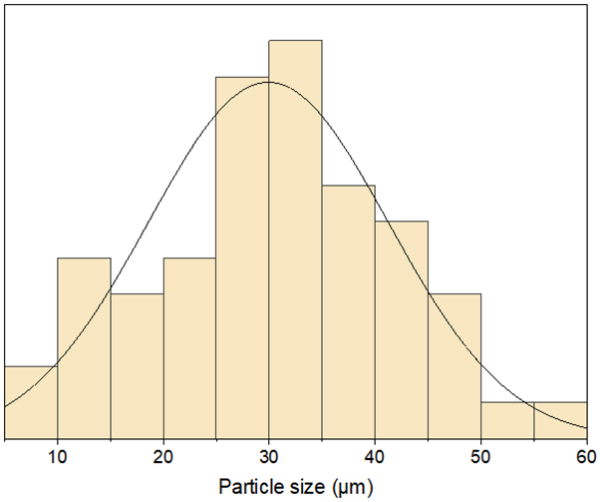

image.

Fig 4.11. Normal distribution of HESA particle size.

The distribution of high entropy superalloy (HESA) particles in aluminum matrix is shown in Fig4.10 using SEM image and corresponding EDS mapping data. Aluminum is present in both the matrix and the reinforcement particles, its considerably low concentration (~9%) in HESA particles compared to Al matrix and other elements in the HESA, causes its color intensity to be extremely low in the EDS elemental map. As seen in SEM image in Fig 4.10, the HESA particles greatly vary in size (10µm-60µm) and this size distribution is depicted in Fig 4.11. using a normal distribution curve. From this plot, it can be observed that the average particle size is around 30µm with a standard deviation of 8.5µm. Particle size is an important parameter to consider as smaller mass to volume ratio of the particles results in greater interaction between the aluminum matrix and HEA particles.

4.2.2 Phase Analysis

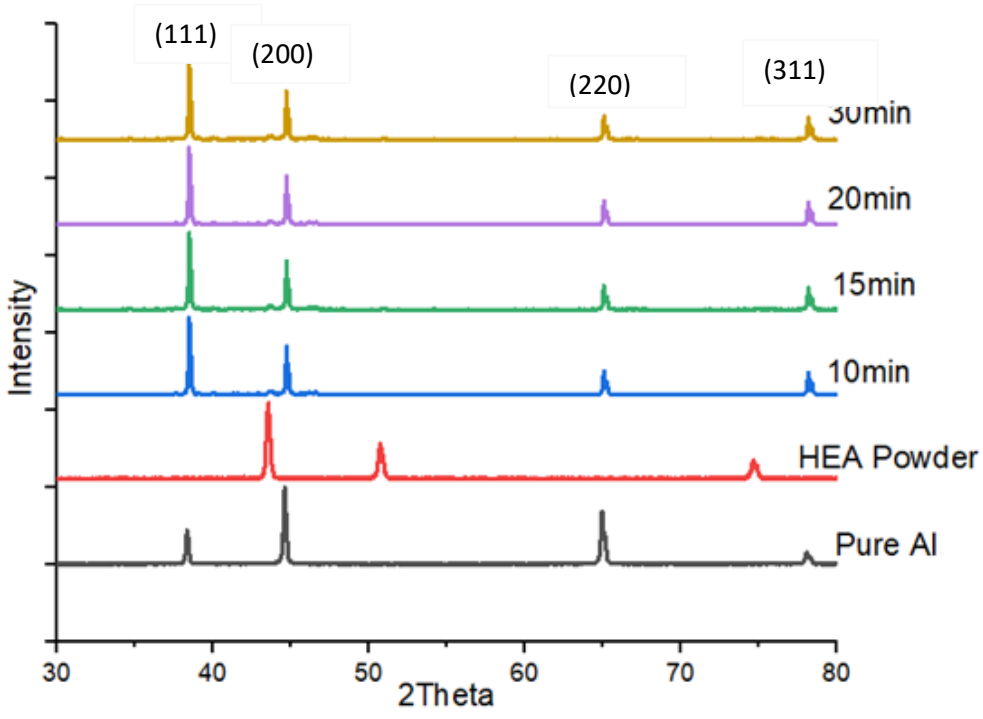

Fig 4.12. X-ray diffraction plot of aluminum, HESA powder and sintered composite specimens.

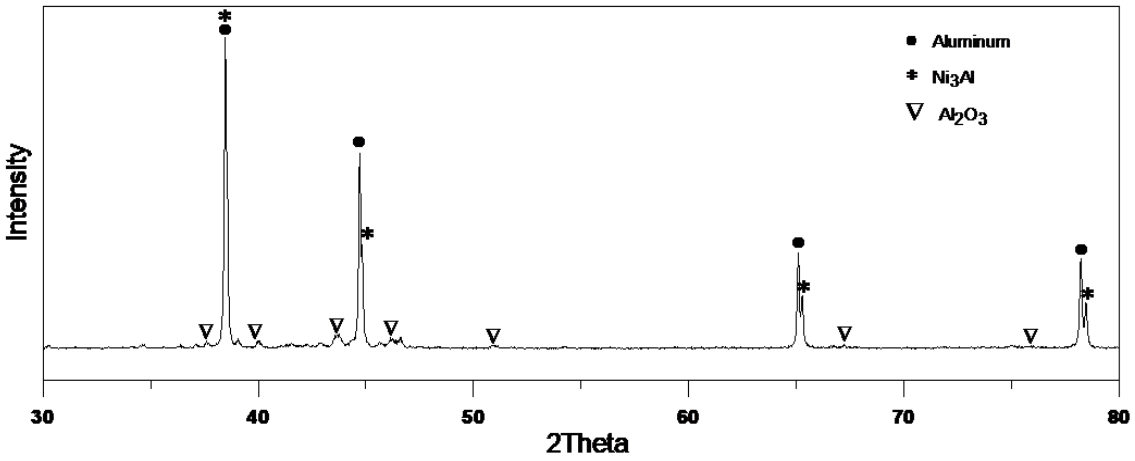

Fig 4.13. Resolved X-ray diffraction plot of HESA/Al composite with holding time 30 min.

It is known that aluminum has FCC crystal structure and previously conducted studies on $Al_{0.5}CoCrFeNi_2$ HESA have also shown the presence of an extremely stable FCC phase in the high entropy alloy. The X-ray diffraction plot shown in Fig 4.12. confirms the above expected phases in Al matrix and HESA reinforcement particles. The elements in $Al_{0.5}CoCrFeNi_2$ are known to dissolve in the Ni lattice thus, the HESA FCC peaks correspond closely with the FCC peaks of nickel. The XRD plot for all sintered Al-HESA composite specimens only showed aluminum peaks as the HESA volume fraction (5vol%) is very small. The Al peaks in composites appear to slightly shift to lower diffraction angle resulting from the distortion in its lattice by addition of reinforcement particles. Fig 4.13 shows an elaborate and magnified XRD plot of composite specimen sintered for 30 min. It can be seen that some minor peaks coinciding with aluminum peaks appear in the XRD plot. Similar observations are also made for remaining sintered composite specimens. These peaks may represent Ni_3Al intermetallic formation in the composites, but advanced analysis needs to be performed in order to confirm this prediction.

4.2.3 Microstructural Analysis of Sintered Composites

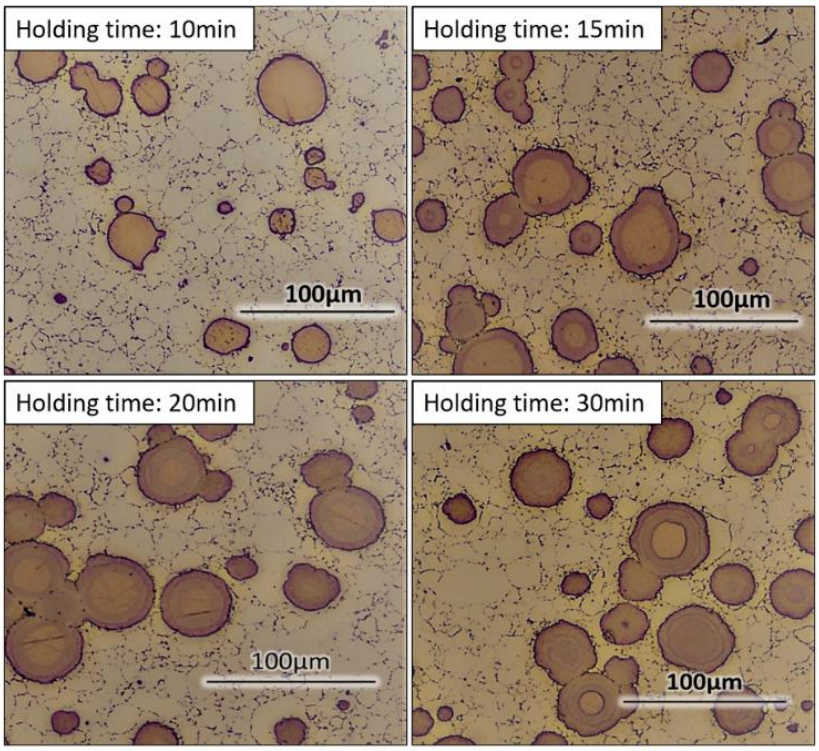

Fig 4.14. Optical Microscopy image of HESA/Al sintered composites.

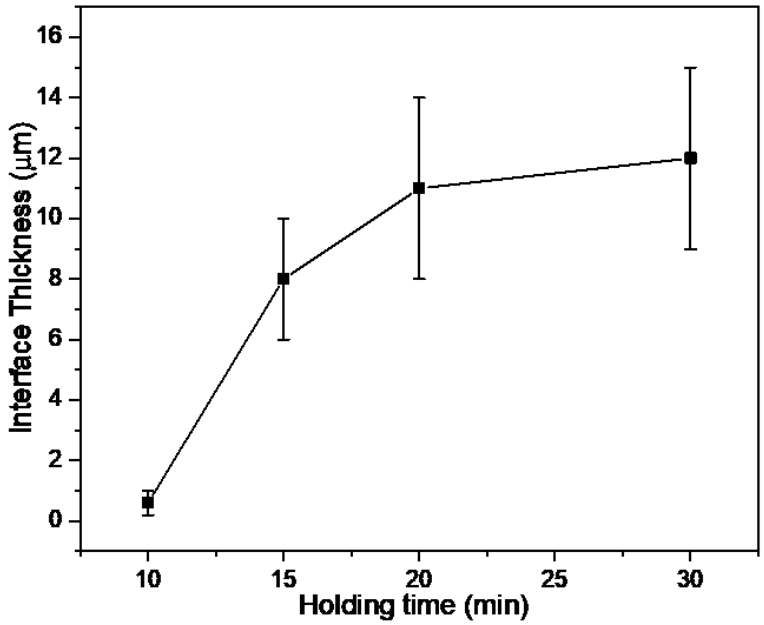

Fig 4.15. Thickness of interdiffusion layer as function of holding time during SPS.

Analysis of aluminum matrix composites with $Al_{0.5}CoCrFeNi_2$ high entropy alloy reinforcement particles using optical microscope as shown in Fig. 4.14 reveals that no interfacial reaction occurs for 10 min holding time. Sintered specimens with a holding time of 15 min and more develop an interdiffusion layer at the interface of the matrix and the reinforcement particles. The growth in the average thickness of the interdiffusion layer as a function of holding time is shown in Fig 4.15. Thus, it can be said that the kinetics of the interfacial reaction come into action between 10 min and 15 min holding time. As mentioned earlier, the HESA particle size varies extensively in the matrix and so does the interfacial reaction and resultant interdiffusion layer growth.

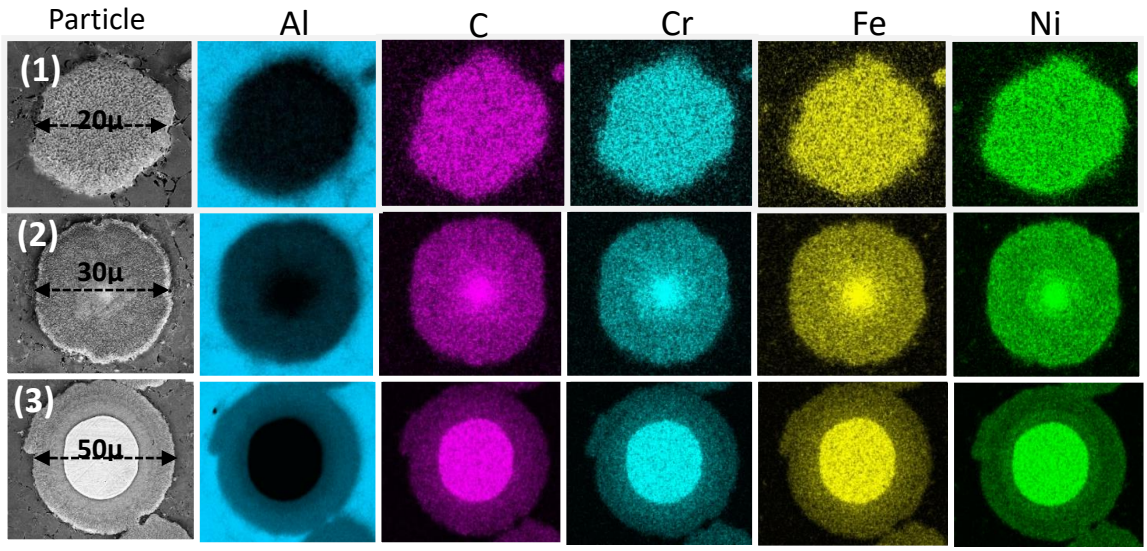

Fig 4.16. Three categories of HESA particles, based on size and corresponding EDS mapping.

Hence, we can divide particles into three different categories as shown in Fig 4.16 including the EDS elemental map of respective particles. The first category of particles involves those which are completely exhausted by the interdiffusion layer and have established a compositional equilibrium with the matrix. No internal compositional gradient is observed in these particles. The second category of particles are the ones which have been almost completely exhausted by the interdiffusion layer. These particles neither have the central HESA core nor have established an equilibrium with the matrix. The interdiffusion reaction has not reached completion in these

particles and as a result of this, an internal gradient exists within the particles. The particles in the first and second category also do not maintain a well-defined spherical shape, and this can be attributed to different diffusion rates of HESA constituent elements in Al matrix. The third category of particles are those which have the original HESA particle at core surrounded by interdiffusion layer in the Al matrix. These particles are around ~35µm or more in size. In these particles, the core region has the same composition as the original HESA particle but the interdiffusion layer shows a gradient in elemental concentration in direction of particle towards Al matrix. Thus, as the interdiffusion reaction is not yet complete and the initial interacting entities still exist, third category particles can be utilized to understand diffusion in the Al-HESA composite system. It is important to note that none of the EDS maps in Fig 4.16 show any elemental segregation in any of the observed regions.

4.2.4 Analysis of Interdiffusion Layer

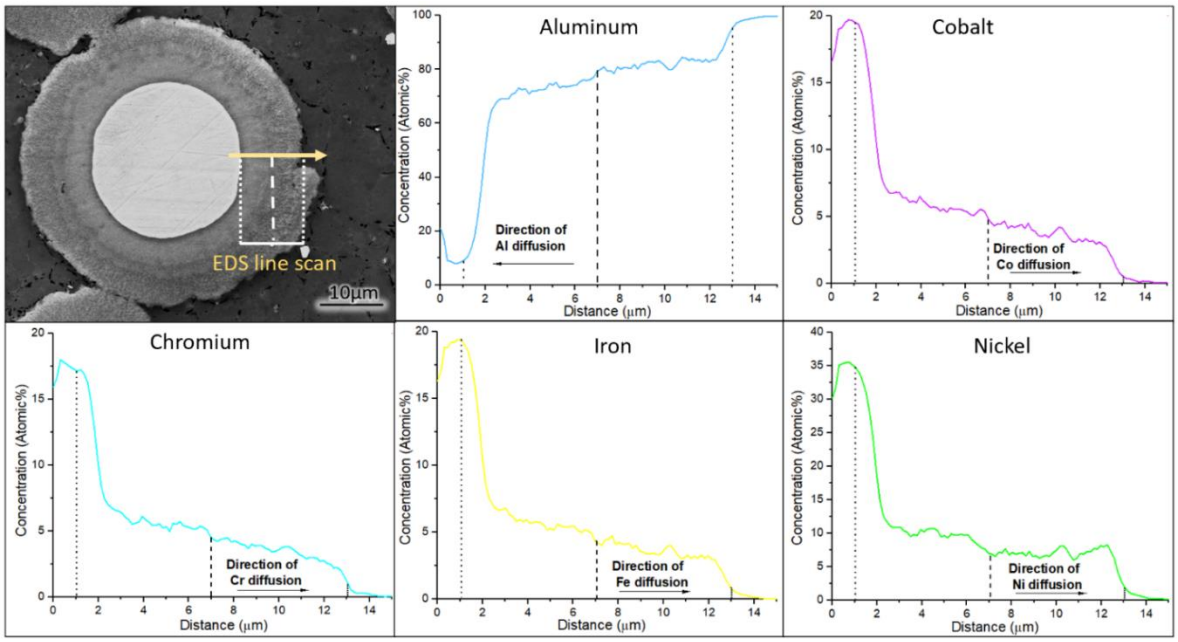

Fig 4.17. EDS line scan of HESA particle in a specimen sintered with 30 min holding time.

In order to understand the diffusion of elements between $Al_{0.5}CoCrFeNi_2$ reinforcement particles and Al matrix, we use the data acquired using EDS line scan. Fig 4.17 shows the EDS line scan of

a third category particle elemental distribution over the following regions- particle, interdiffusion layer and the matrix. To define the physical boundaries for diffusion study we first analyze the physical morphology of the interdiffusion layer. In Fig 4.17, it can be observed in the image of the particle that the interdiffusion layer has a central division boundary separating the inner smooth region and outer rough region of the interdiffusion layer. We assume that this central separating line in the interdiffusion layer is the original boundary line of the HESA particle. Aluminum would diffusion inwards into the HESA particle crossing this boundary line with uniform diffusivity into the material forming a smoother region. In contrast, cobalt, chromium, iron and nickel diffuse outwards towards the aluminum matrix across the boundary line at different rates resulting in a rough outer layer. After analyzing the ID layer in multiple large HESA particles, it was found that this boundary line always maintains the equilibrium concentration which the reinforcement particle intends to achieve as result of diffusion. The approximate equilibrium concentration of Al, Co, Cr, Fe and Ni are 80at%, 4.4at%, 4.3at%,4.2at% and 7at% respectively. From the EDS line scan data in Fig 4.17, we acquire the concentration gradient of Al, Co, Cr, Fe and Ni over the interdiffusion layer region. It must be noted that the diffusion of Co, Cr, Fe, Ni towards Al matrix appears to occur in a proportionate manner corresponding to their initial concentration in the HESA particle. Al on other hand, dominates the elemental demographic in the interdiffusion layer with concentration ranging from 65at% to 85at%. The slopes of all elements in the interdiffusion layer do not indicate any form of segregation occurring in this region. Hence, we can infer that the interdiffusion layer is an aluminum alloy with a large concentration of alloying elements. The diffusion at interface appears to be controlled by vacancy mechanism during spark plasma sintering.

4.2.5 Nanoindentation

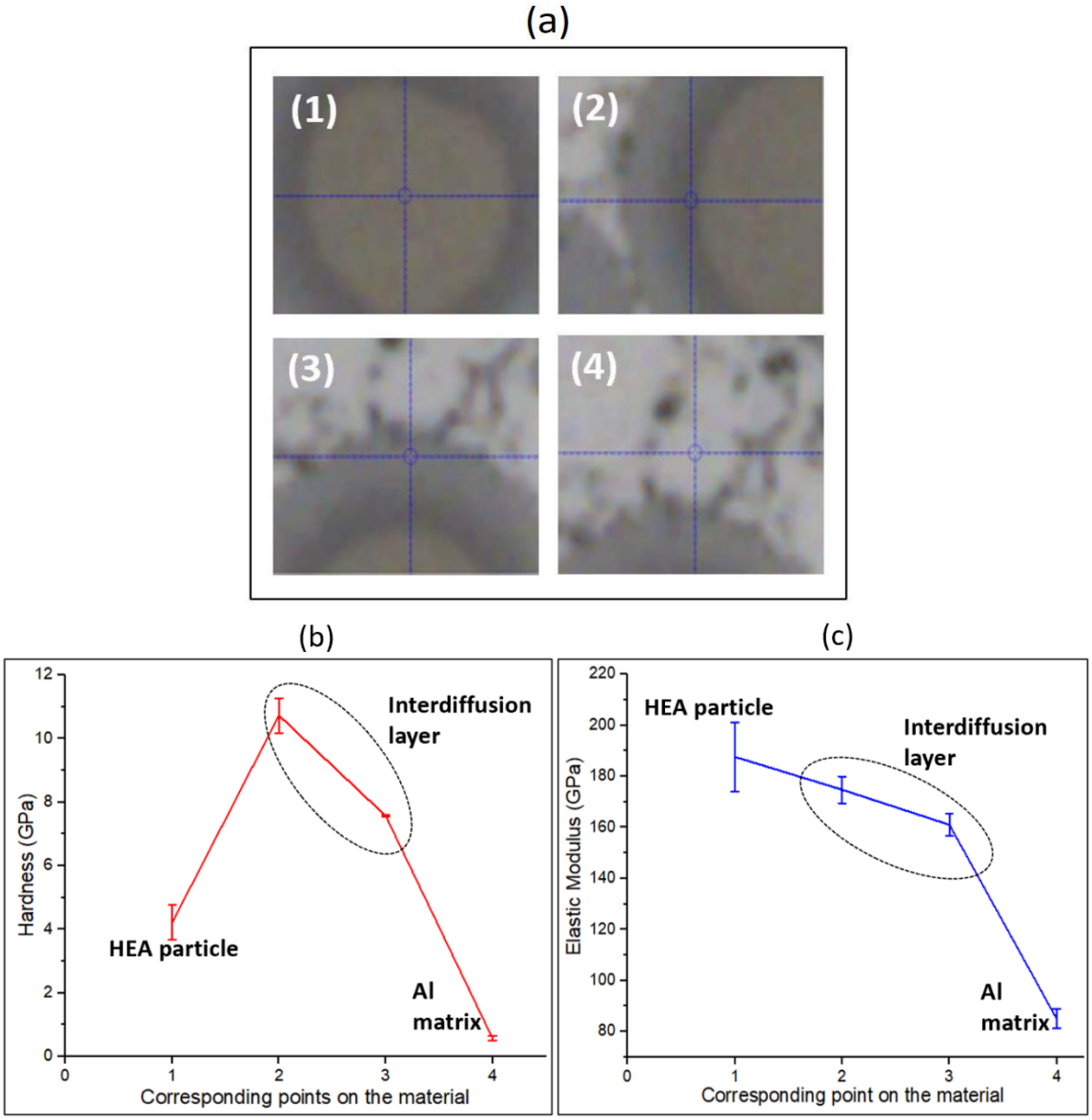

Fig 4.18. (a) Areas selected for nanoindentation, (b) Hardness (c) Elastic Modulus of the corresponding points.

The interface of the matrix and reinforcement in a composite material governs its properties. In this case, analyzing the mechanical properties of the interdiffusion layer with respect to the HESA particle and Al matrix will allow us to better predict the overall composite properties. For this purpose, nanoindentation was performed on the HESA particle, smooth and rough region of

the interdiffusion layer and the Al matrix. Fig 4.18a shows the regions that were chosen to perform nanoindentation test and the hardness and elastic modulus calculated from the test are presented in Fig 4.18b and Fig 4.18c respectively. The HESA particles have a hardness of 4.22GPa, followed by the inner region and outer region of interdiffusion layer showcasing hardness values of 10.73GPa and 7.57GPa respectively. The softer aluminum matrix recorded a hardness of 0.57GPa. Observing the trend in hardness values, it is clear that the interdiffusion layer region has much higher hardness in the inner and outer region compared to both the HESA particle and the Al matrix. Comparing trend in the hardness values against the trend observed in elastic modulus values of the same regions, the elastic modulus decreases from the particle through the interface towards the matrix region. Elastic modulus is a material property and is insensitive to strengthening treatments. Thus, to explain the trend observed for hardness data, we consider a possibility of precipitation hardening. Although not observed in the EDS data, XRD results do show peaks Ni_3Al intermetallic in the composites. Therefore, we may expect that Ni_3Al intermetallic precipitate is formed in the interdiffusion layer region causing a spike in hardness. This might also explain why the trend in elastic modulus did not agree with that observed for hardness. In order to prove the formation of this intermetallic and predict its composition, we conducted TEM analysis of the composite material.

4.2.6 TEM Analysis of Interdiffusion Layer:

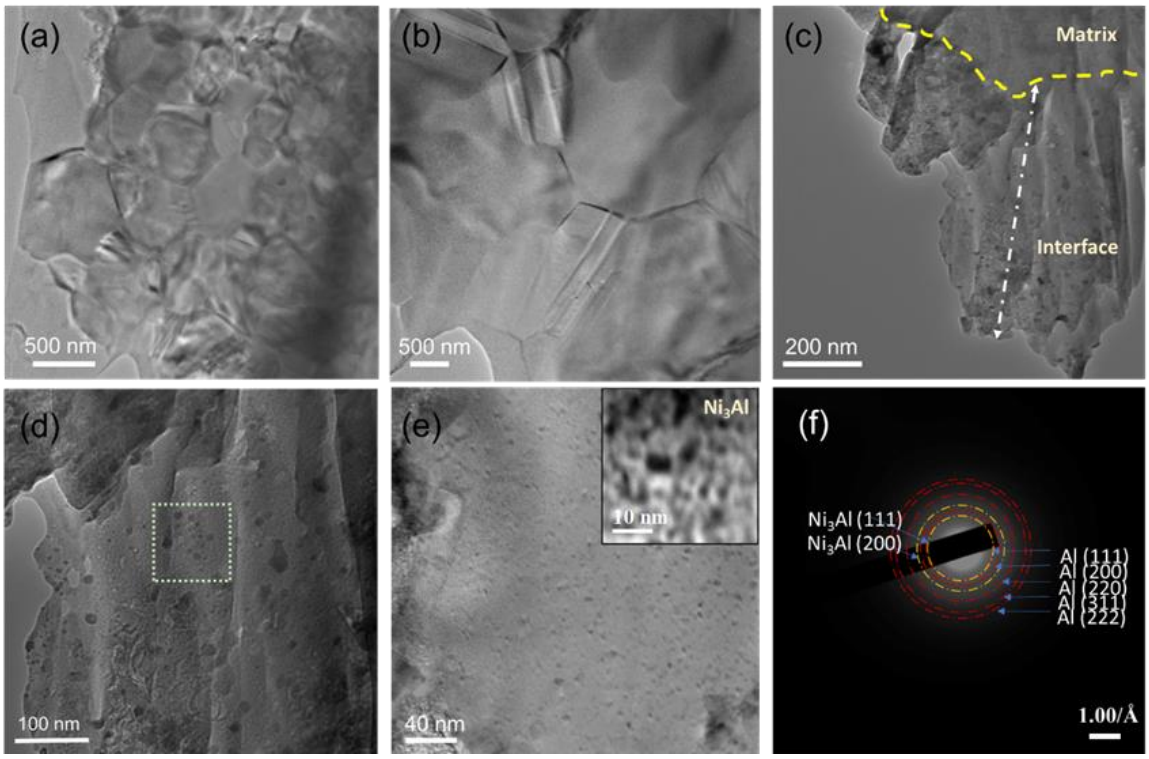

Figure 4.19. (a) TEM image revealing grains in Al-HEA composites. (b) Magnified TEM image having average grain size of ~2-3 µm. (c) TEM image showing the interface area of the consumed HEA particle. (d) Representative image of the interface area showing formation of nano-precipitates. (e) Magnified image of the selected area from (d), and the inset image shows Ni_3Al precipitates. (f) SAED pattern of the Al-HEA composites.

Fig 4.19(a) shows the TEM image of Al-HEA composites. Here, we are able to clearly see the grains of the Al-HEA composites. Higher magnification images of these grains were acquired to further understand the morphology of these grains. The average grain size measured is ~2-3 µm. These grains show the formation of nano-twins, as shown in Fig 4.19(b). The study was conducted at Al-HEA interface to understand the phase segregation. The matrix and the interface are marked in Fig 4.19(c). These regions could be clearly distinguished based on the Z-contrast. This is due to the presence of heavy elements such as Ni, Co, Cr, and Fe at the interface while matrix is being Al. Fig 4.19(d) shows the TEM image of the interface revealed the presence of

precipitates. Further study at the selected area as shown in Fig 4.19(d) was carried out at further higher magnifications. Fig 4.19(e) depicts uniform distribution of the nanoprecipitates in the interface region. The inset image in Fig 4.19(e) is taken at a very high magnification shows that the average size of nanoprecipitates ~2-4 nm. The nanoprecipitates show faceted structure and they are further confirmed as Ni_3Al using SAED pattern. The SAED patterns were indexed using FCC-Al (space group $Fm\bar{3}m$) and standard cubic Ni_3Al (space group $Pm\bar{3}m$) phase. The lattice parameters of Al (a = 4.04 Å and c = 4.04 Å) and Ni_3Al[68] (a = 3.52 Å and c = 3.52 Å) were used for identifying planar spacing. The SAED pattern illustrates ring pattern formation of Al which are indexed as (111), (200), (220), (311) and (222) respectively. In addition, diffraction rings corresponding to (111) and (200) reflections of Ni_3Al were also identified. These indexed planes are analogous to earlier reported literature[69]–[71].

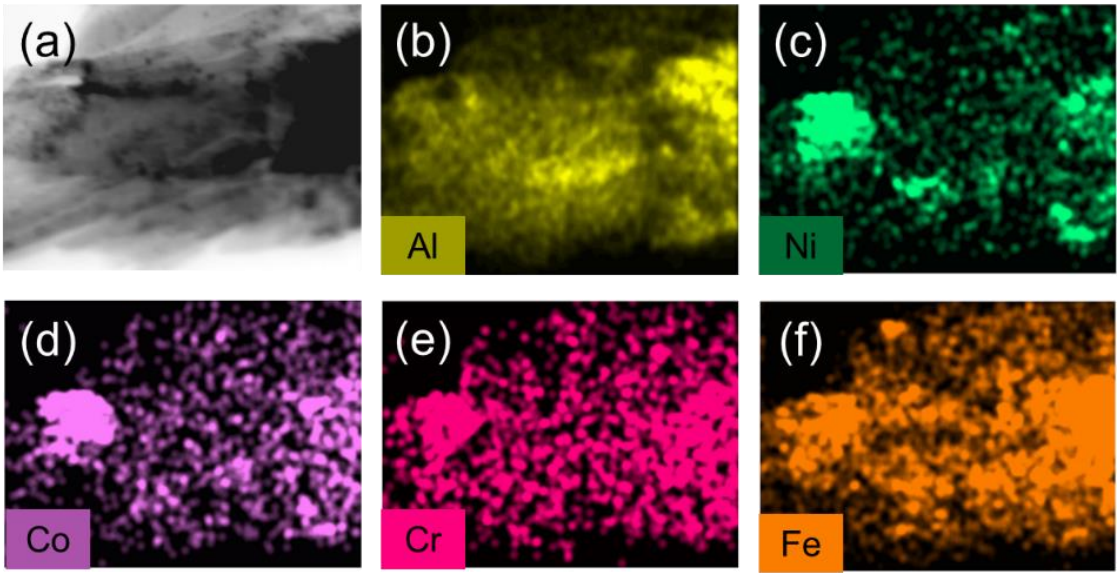

Figure 4.20. (a) TEM image of the Al-HEA interface for acquiring EDS maps. (b-f) EDS maps showing distribution of Al, Ni, Co, Cr, and Fe respectively.

Figure 4.20(a) Shows TEM image from the interface region. The EDS analysis was done on the corresponding region for elemental mapping. The maps (b-f) show the distribution of the elements. From the above EDS mapping we can conclude the intermixing of elements from the matrix and HEA in the interface.

4.2.7 Wear Analysis:

As confirmed by TEM analysis, Ni_3Al nanoprecipitates are formed in the interdiffusion layer. The precipitation of Ni_3Al is commonly observed in nickel superalloys where it acts as a strengthening phase. Thus, we can state that due to destabilization of HESA and diffusion at interface, it reinstates the characteristics of the parent conventional superalloy. The precipitation of Ni_3Al in ID layer region greatly affects the load transfer behavior of the reinforcement-matrix system. If the composite system shows a hardness trend as reinforcement > interface > matrix, it can ideally allow the matrix to transfer the load to the reinforcement via interface region resulting into strengthening of the matrix. But in the Al-HESA composite system, hardness of interface > HESA particle > Al matrix. When load is applied on this system, the interdiffusion layer will

inadequately transfer load from the matrix to the reinforcement. With hardness of interdiffusion layer being higher than both the HESA particle and Al matrix, it becomes a stress concentration region in the composites and can reduce the plasticity of the material.

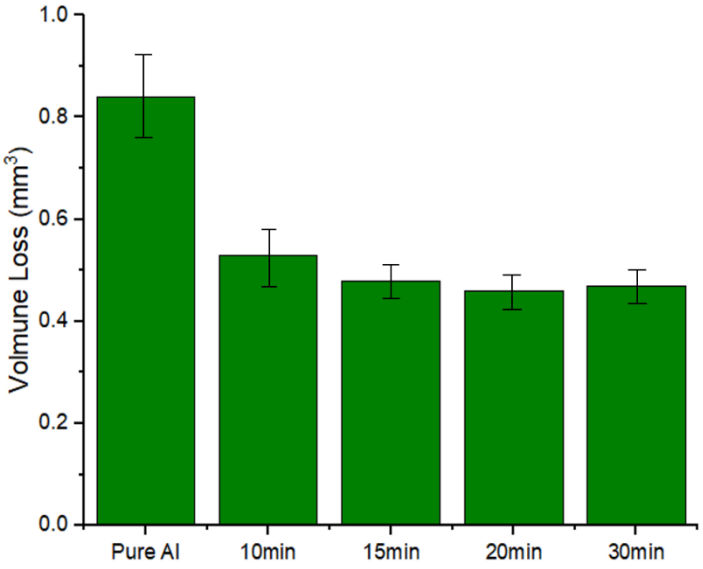

Fig 4.21. Volumetric wear loss with respect to holding time of sintered composite specimens.

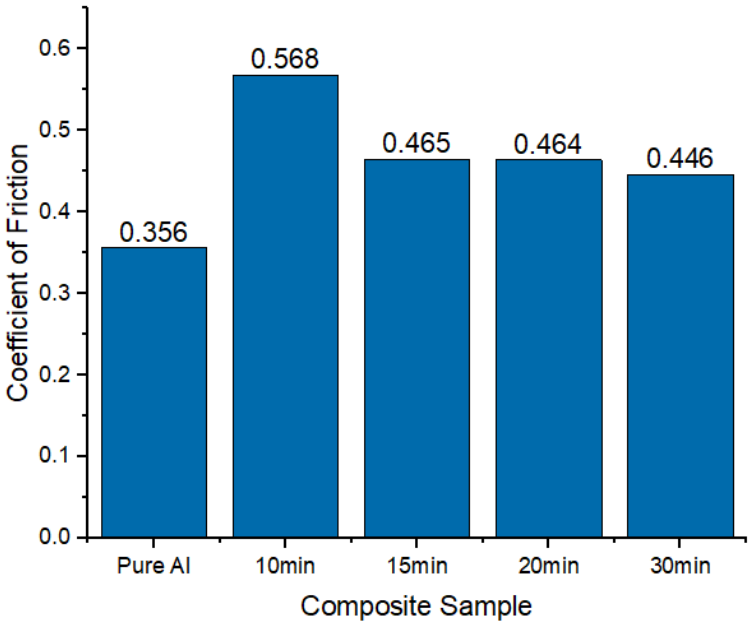

Fig 4.22. Coefficient of friction with respect to holding time of sintered composite specimens.

The results of the ball on disk wear test are shown in Fig 4.21 and Fig 4.22. Comparing the wear loss of sintered pure aluminum and sintered Al-HESA composite specimens, it is observed that Pure Al has the highest wear loss in terms of material volume. The wear significantly reduces in 10 min sintered composite specimen in comparison to pure Al. Even with absence of an interdiffusion layer in 10 min sintered specimen, the HESA particles appear to hold the matrix and oppose deformation. All other sintered Al-HESA composite specimens exhibited slightly lower wear loss than that of 10min specimen. For sintered specimens with holding time 15 min, 20 min and 30 min the wear rate appears to be comparable irrespective of the thickness of the interdiffusion layer. Pure Al had the lowest coefficient of friction and the Al-HESA specimen sintered for 10min had the highest coefficient of friction. The 15 min, 20 min and 30 min sintered specimens recorded very similar values of coefficient of friction which was higher than pure Al but lower than 10min sintered specimen. To better understand the reasons for this trends, we analyzed the wear tracks of pure Al and all sintered specimens using SEM. Pure Al, being a soft metal, exhibits adhesive wear leading to excessive volumetric loss during wear. The Al-HESA sintered specimen with a holding time of 10min does not have an interdiffusion layer formed around HESA particles. Therefore, the reinforcement particles, although holding the matrix, are not strongly bonded with it. During wear, these particles are easily debonded and act as a third body wear medium. As a result of this, the 10 min specimen exhibits third body assisted adhesive wear and leads to greater wear loss compared to 15 min, 20 min and 30 min specimens, and a higher value of coefficient of friction.

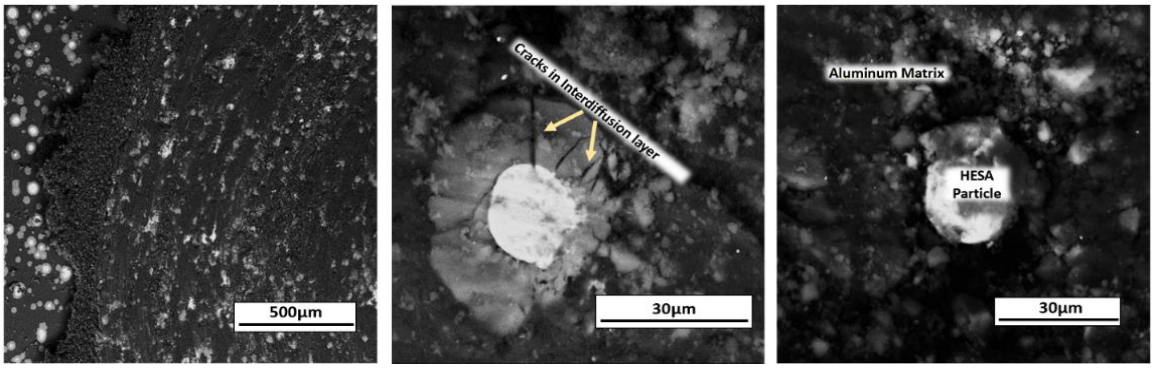

Fig 4.23. SEM images of wear track of specimen with holding time 30min.

The SEM images shown in Fig 4.23 help us understand the effect of interdiffusion layer on wear behavior of 15 min, 20 min and 30 min specimens. As seen in the images below, the interdiffusion layer seems to have developed cracks during wear test, followed by detachment of the HESA particle from the matrix. This aligns with the previously made discussion that the interface of HESA and aluminum act as stress concentration zone due to nanoprecipitate formation during sintering process. Therefore, the interdiffusion layer becomes brittle and displays a reduced particle holding capacity.

CHAPTER V

CONCLUSIONS

5.1 Analysis of $Al_{0.5}CoCrFeNi_2$ processed by Spark Plasma Sintering

The $Al_{0.5}CoCrFeNi_2$ high entropy superalloy powder and all the sintered specimens have a stable single phase FCC crystal structure. The stability of FCC phase in $Al_{0.5}CoCrFeNi_2$ HESA over a wide range of sintering temperature can be attributed to high configurational entropy and cocktail effect. The use of gas atomized powder particles used for sintering resulted in pronounced porosity pinning effect. Spheroidization of porosities was needed to overcome the pinning effect and achieve complete densification. The diffusion of elements on surface and bonding of powder particles and consequent porosity elimination can be achieved by sintering temperature. The hardness of the high entropy super alloy was found to be 245±5HV. Hardness does not appear to be impacted by change in grain size. Formation of precipitates in Ni-superalloys increases wear resistance of the material but the absence of these precipitates results - in softer and more wear susceptible $Al_{0.5}CoCrFeNi_2$ HESA. Adhesive wear, delamination, oxidation wear and minor signs of abrasive wear are thus, visible in the high entropy superalloy with the coefficient of friction lying in the range of 0.6-0.7.

5.2 Interdiffusion Layer Formation and Wear properties of Al/$Al_{0.5}CoCrFeNi_2$ Composites

Al/$Al_{0.5}CoCrFeNi_2$ composites were successfully processed using spark plasma sintering. The following conclusions were derived from analysis- the interface reaction happens between the holding time of 10 min and 15 min. Smaller HESA particles get rapidly consumed by the interdiffusion layer to develop a chemically inhomogeneous region in the aluminum matrix. The diffusion reaction continues to reach an equilibrium between the HESA particle and Al matrix. The destabilization of $Al_{0.5}CoCrFeNi_2$ HESA and interface diffusion leads to formation of Ni_3Al intermetallic precipitates in the interdiffusion layer region. This results in precipitation hardening of the interface making it a stress concentration zone. Cracking of interdiffusion layer during wear test proves the brittle nature of it and reduced ability to transfer load between the matrix and reinforcement. If the formation of Ni_3Al can be controlled, Al/ $Al_{0.5}CoCrFeNi_2$ composites have the potential to exhibit superior mechanical properties making it an attractive material for structural applications.

REFERENCES AND PUBLICATION

References:

[1] J. W. Yeh, Y. L. Chen, S. J. Lin, and S. K. Chen, "High-Entropy Alloys – A New Era of Exploitation," *Mater. Sci. Forum*, vol. 560, pp. 1–9, 2007, doi: 10.4028/www.scientific.net/msf.560.1.

[2] M. H. Tsai and J. W. Yeh, "High-entropy alloys: A critical review," *Mater. Res. Lett.*, vol. 2, no. 3, pp. 107–123, 2014, doi: 10.1080/21663831.2014.912690.

[3] S. Chikumba and V. V. Rao, "High Entropy Alloys: Development and Applications," *7th Int. Conf. Latest Trends Eng. Technol. Nov. 26-27*, pp. 1–5, 2015, doi: 10.15242/iie.e1115005.

[4] R. Chen, G. Qin, H. Zheng, L. Wang, Y. Su, Y. L. Chiu, H. Ding, J. Guo, and H. Fu, "Composition design of high entropy alloys using the valence electron concentration to balance strength and ductility," *Acta Mater.*, vol. 144, no. October, pp. 129–137, 2018, doi: 10.1016/j.actamat.2017.10.058.

[5] O. N. Senkov, G. B. Wilks, D. B. Miracle, C. P. Chuang, and P. K. Liaw, "Refractory high-entropy alloys," *Intermetallics*, vol. 18, no. 9, pp. 1758–1765, 2010, doi: 10.1016/j.intermet.2010.05.014.

[6] J. Chen, X. Zhou, W. Wang, B. Liu, Y. Lv, D. Xu, W. Yang, and Y. Liu, "Corrigendum to 'A review on fundamental of high entropy alloys with promising high–temperature properties' [J. Alloys Compd. 760 (2018) 15–30] (Journal of Alloys and Compounds (2018) 760 (15–30), (S092583881831747X), (10.1016/j.jallcom.2018.05.067))," *J. Alloys Compd.*, vol. 785, p. 1294, 2019, doi: 10.1016/j.jallcom.2019.01.386.

[7] R. Feng, M. C. Gao, C. Lee, M. Mathes, T. Zuo, S. Chen, J. A. Hawk, Y. Zhang, and P. K. Liaw, "Design of light-weight high-entropy alloys," *Entropy*, vol. 18, no. 9, pp. 16–29, 2016, doi: 10.3390/e18090333.

[8] O. Maulik, D. Kumar, S. Kumar, S. K. Dewangan, and V. Kumar, "Structure and properties of lightweight high entropy alloys: A brief review," *Mater. Res. Express*, vol. 5, no. 5, 2018, doi: 10.1088/2053-1591/aabbca.

[9] A. Kumar and M. Gupta, "An insight into evolution of light weight high entropy alloys: A review," *Metals (Basel).*, vol. 6, no. 9, 2016, doi: 10.3390/met6090199.

[10] Z. Li and D. Raabe, “Strong and Ductile Non-equiatomic High-Entropy Alloys: Design, Processing, Microstructure, and Mechanical Properties,” *Jom*, vol. 69, no. 11, pp. 2099–2106, 2017, doi: 10.1007/s11837-017-2540-2.

[11] K. Lu, “The future of metals,” *Science (80-.).*, vol. 328, no. 5976, pp. 319–320, 2010, doi: 10.1126/science.1185866.

[12] M. Krasnowski and T. Kulik, “Nanocrystalline Al-Fe intermetallics - light weight alloys with high hardness,” *Intermetallics*, vol. 18, no. 1, pp. 47–50, 2010, doi: 10.1016/j.intermet.2009.06.006.

[13] J. C. Williams and E. A. Starke, “Progress in structural materials for aerospace systems,” *Acta Mater.*, vol. 51, no. 19, pp. 5775–5799, 2003, doi: 10.1016/j.actamat.2003.08.023.

[14] D. B. Miracle, “Metal matrix composites - From science to technological significance,” *Compos. Sci. Technol.*, vol. 65, no. 15-16 SPEC. ISS., pp. 2526–2540, 2005, doi: 10.1016/j.compscitech.2005.05.027.

[15] S. Li, K. Kondoh, H. Imai, B. Chen, L. Jia, J. Umeda, and Y. Fu, “Strengthening behavior of in situ-synthesized (TiC-TiB)/Ti composites by powder metallurgy and hot extrusion,” *Mater. Des.*, vol. 95, pp. 127–132, 2016, doi: 10.1016/j.matdes.2016.01.092.

[16] D. R. Ni, L. Geng, J. Zhang, and Z. Z. Zheng, “Effect of B4C particle size on microstructure of in situ titanium matrix composites prepared by reactive processing of Ti-B4C system,” *Scr. Mater.*, vol. 55, no. 5, pp. 429–432, 2006, doi: 10.1016/j.scriptamat.2006.05.024.

[17] X. Guo, Q. Guo, J. Nie, Z. Liu, Z. Li, G. Fan, D. B. Xiong, Y. Su, J. Fan, and D. Zhang, “Particle size effect on the interfacial properties of SiC particle-reinforced Al-Cu-Mg composites,” *Mater. Sci. Eng. A*, vol. 711, no. November 2017, pp. 643–649, 2018, doi: 10.1016/j.msea.2017.11.068.

[18] C. Si, X. Tang, X. Zhang, J. Wang, and W. Wu, “Microstructure and mechanical properties of particle reinforced metal matrix composites prepared by gas-solid two-phase atomization and deposition technology,” *Mater. Lett.*, vol. 201, pp. 78–81, 2017, doi: 10.1016/j.matlet.2017.04.150.

[19] E. Akca and A. Gürsel, “A Review on Superalloys and IN718 Nickel-Based INCONEL Superalloy,” *Period. Eng. Nat. Sci.*, vol. 3, no. 1, 2015, doi: 10.21533/pen.v3i1.43.

[20] G. R. Thellaputta, P. S. Chandra, and C. S. P. Rao, “Machinability of Nickel Based Superalloys: A Review,” *Mater. Today Proc.*, vol. 4, no. 2, pp. 3712–3721, 2017, doi: 10.1016/j.matpr.2017.02.266.

[21] L. Zhang, Y. Zhou, X. Jin, X. Du, and B. Li, “The microstructure and high-temperature properties of novel nano precipitation-hardened face centered cubic high-entropy superalloys,” *Scr. Mater.*, vol. 146, pp. 226–230, 2018, doi: 10.1016/j.scriptamat.2017.12.001.

[22] Y. T. Chen, Y. J. Chang, H. Murakami, T. Sasaki, K. Hono, C. W. Li, K. Kakehi, J. W. Yeh, and A. C. Yeh, “Hierarchical microstructure strengthening in a single crystal high entropy superalloy,” *Sci. Rep.*, vol. 10, no. 1, pp. 1–11, 2020, doi: 10.1038/s41598-020-69257-8.

[23] T. K. Tsao, A. C. Yeh, C. M. Kuo, K. Kakehi, H. Murakami, J. W. Yeh, and S. R. Jian, "The High Temperature Tensile and Creep Behaviors of High Entropy Superalloy," *Sci. Rep.*, vol. 7, no. 1, pp. 1–9, 2017, doi: 10.1038/s41598-017-13026-7.

[24] A. Yeh, T. Tsao, Y. Chang, K. Chang, J. Yeh, M. Chiou, S. Jian, C. Kuo, W. Wang, and H. Murakami, "Developing New Type of High Temperature Alloys–High Entropy Superalloys," *Int. J. Metall. Mater. Eng.*, vol. 1, no. 1, pp. 1–4, 2015.

[25] Y. T. Chen, Y. J. Chang, H. Murakami, S. Gorsse, and A. C. Yeh, "Designing high entropy superalloys for elevated temperature application," *Scr. Mater.*, vol. 187, pp. 177–182, 2020, doi: 10.1016/j.scriptamat.2020.06.002.

[26] Surappa M.K., "Aluminium Matrix Composites: Challenges and Opportunities // Sadhana. Department of Metallurgy, Indian Institute of Science, Bangalore 560 012, India," *S¯adhan¯a*, vol. 28, no. 1–2, pp. 319–334, 2003.

[27] S. Attar, M. Nagaral, H. N. Reddappa, and V. Auradi, "A Review on Particulate Reinforced Aluminum Metal Matrix Composites," *J. Emerg. Technol. Innov. Res.*, vol. 2, no. 2, pp. 225–229, 2015.

[28] S. T. Mavhungu, E. T. Akinlabi, M. A. Onitiri, and F. M. Varachia, "Aluminum Matrix Composites for Industrial Use: Advances and Trends," *Procedia Manuf.*, vol. 7, pp. 178–182, 2017, doi: 10.1016/j.promfg.2016.12.045.

[29] D. K. Koli, G. Agnihotri, and R. Purohit, "Advanced Aluminium Matrix Composites: The Critical Need of Automotive and Aerospace Engineering Fields," *Mater. Today Proc.*, vol. 2, no. 4–5, pp. 3032–3041, 2015, doi: 10.1016/j.matpr.2015.07.290.

[30] M. G. de Cortázar, P. Egizabal, J. Barcena, and Y. Le Petitcorps, "Metal Matrix Composites," *Struct. Mater. Process. Transp.*, no. April, pp. 303–338, 2013, doi: 10.1002/9783527649846.ch9.

[31] Z. Shi, J. M. Yang, J. C. Lee, D. Zhang, H. I. Lee, and R. Wu, "The interfacial characterization of oxidized SiC(p)/2014 A1 composites," *Mater. Sci. Eng. A*, vol. 303, no. 1–2, pp. 46–53, 2001, doi: 10.1016/S0921-5093(00)01943-2.

[32] K. Ravi Kumar, T. Pridhar, and V. S. Sree Balaji, "Mechanical properties and characterization of zirconium oxide (ZrO2) and coconut shell ash(CSA) reinforced aluminium (Al 6082) matrix hybrid composite," *J. Alloys Compd.*, vol. 765, pp. 171–179, 2018, doi: 10.1016/j.jallcom.2018.06.177.

[33] R. F. Guo, N. Guo, P. Shen, L. K. Yang, and Q. C. Jiang, "Effects of ceramic lamellae compactness and interfacial reaction on the mechanical properties of nacre-inspired Al/Al2O3–ZrO2 composites," *Mater. Sci. Eng. A*, vol. 718, no. February, pp. 326–334, 2018, doi: 10.1016/j.msea.2018.01.088.

[34] L. Zhang, L. K. Yang, J. Leng, T. Wang, and Y. Wang, "Alloying Behavior and Properties of Al-Based Composites Reinforced with Al85Fe15 Metallic Glass Particles Fabricated by Mechanical Alloying and Hot Pressing Consolidation," *Jom*, vol. 69, no. 4, pp. 748–755, 2017, doi: 10.1007/s11837-016-2239-9.

[35] H. Kato, H. S. Chen, and A. Inoue, "Relationship between thermal expansion coefficient and glass transition temperature in metallic glasses," *Scr. Mater.*, vol. 58, no. 12, pp.

1106–1109, 2008, doi: 10.1016/j.scriptamat.2008.02.006.

[36] Z. Yuan, H. Liu, Z. Ma, X. Ma, K. Wang, and X. Zhang, “Microstructure and properties of high entropy alloy reinforced titanium matrix composites,” *Mater. Charact.*, vol. 187, no. March, p. 111856, 2022, doi: 10.1016/j.matchar.2022.111856.

[37] J. Chen, P. Niu, T. Wei, L. Hao, Y. Liu, X. Wang, and Y. Peng, “Fabrication and mechanical properties of AlCoNiCrFe high-entropy alloy particle reinforced Cu matrix composites,” *J. Alloys Compd.*, vol. 649, pp. 630–634, 2015, doi: 10.1016/j.jallcom.2015.07.125.

[38] C. Zhang, J. Zhu, C. Ji, Y. Guo, R. Fang, S. Mei, and S. Liu, “Laser powder bed fusion of high-entropy alloy particle-reinforced stainless steel with enhanced strength, ductility, and corrosion resistance,” *Mater. Des.*, vol. 209, p. 109950, 2021, doi: 10.1016/j.matdes.2021.109950.

[39] N. Wang, B. Wu, W. Wu, J. Li, C. Ge, Y. Dong, L. Zhang, and Y. Wang, “Microstructure and properties of aluminium-high entropy alloy composites fabricated by mechanical alloying and spark plasma sintering,” *Mater. Today Commun.*, vol. 25, no. June, pp. 1–8, 2020, doi: 10.1016/j.mtcomm.2020.101366.

[40] G. M. Karthik, S. Panikar, G. D. J. Ram, and R. S. Kottada, “Additive manufacturing of an aluminum matrix composite reinforced with nanocrystalline high-entropy alloy particles,” *Mater. Sci. Eng. A*, vol. 679, no. September 2016, pp. 193–203, 2017, doi: 10.1016/j.msea.2016.10.038.

[41] Y. Liu, J. Chen, Z. Li, X. Wang, X. Fan, and J. Liu, “Formation of transition layer and its effect on mechanical properties of AlCoCrFeNi high-entropy alloy/Al composites,” *J. Alloys Compd.*, vol. 780, pp. 558–564, 2019, doi: 10.1016/j.jallcom.2018.11.364.

[42] Z. Yuan, W. Tian, F. Li, Q. Fu, X. Wang, W. Qian, and W. An, “Effect of heat treatment on the interface of high-entropy alloy particles reinforced aluminum matrix composites,” *J. Alloys Compd.*, vol. 822, no. 2020, p. 153658, 2020, doi: 10.1016/j.jallcom.2020.153658.

[43] Y. Zhang, X. Li, H. Gu, R. Li, P. Chen, C. Kong, and H. Yu, “Insight of high-entropy alloy particles-reinforced 2219 Al matrix composites via the ultrasonic casting technology,” *Mater. Charact.*, vol. 182, no. October, p. 111548, 2021, doi: 10.1016/j.matchar.2021.111548.

[44] Z. Yuan, W. Tian, F. Li, Q. Fu, Y. Hu, and X. Wang, “Microstructure and properties of high-entropy alloy reinforced aluminum matrix composites by spark plasma sintering,” *J. Alloys Compd.*, vol. 806, no. 2019, pp. 901–908, 2019, doi: 10.1016/j.jallcom.2019.07.185.

[45] J. Li, Y. Li, F. Wang, X. Meng, L. Wan, Z. Dong, and Y. Huang, “Friction stir processing of high-entropy alloy reinforced aluminum matrix composites for mechanical properties enhancement,” *Mater. Sci. Eng. A*, vol. 792, no. June, p. 139755, 2020, doi: 10.1016/j.msea.2020.139755.

[46] N. Saheb, Z. Iqbal, A. Khalil, A. S. Hakeem, N. Al Aqeeli, T. Laoui, A. Al-Qutub, and R. Kirchner, “Spark plasma sintering of metals and metal matrix nanocomposites: A review,” *J. Nanomater.*, vol. 2012, 2012, doi: 10.1155/2012/983470.

[47] V. Mamedov, “Spark plasma sintering as advanced PM sintering method,” *Powder Metall.*, vol. 45, no. 4, pp. 322–328, 2002, doi: 10.1179/003258902225007041.

[48] Z. A. Munir, U. Anselmi-Tamburini, and M. Ohyanagi, “The effect of electric field and pressure on the synthesis and consolidation of materials: A review of the spark plasma sintering method,” *J. Mater. Sci.*, vol. 41, no. 3, pp. 763–777, 2006, doi: 10.1007/s10853-006-6555-2.

[49] Z. Y. Hu, Z. H. Zhang, X. W. Cheng, F. C. Wang, Y. F. Zhang, and S. L. Li, “A review of multi-physical fields induced phenomena and effects in spark plasma sintering: Fundamentals and applications,” *Mater. Des.*, vol. 191, p. 108662, 2020, doi: 10.1016/j.matdes.2020.108662.

[50] A. Zhang, J. Han, J. Meng, B. Su, and P. Li, “Rapid preparation of AlCoCrFeNi high entropy alloy by spark plasma sintering from elemental powder mixture,” *Mater. Lett.*, vol. 181, pp. 82–85, 2016, doi: 10.1016/j.matlet.2016.06.014.

[51] S. H. Joo, H. Kato, M. J. Jang, J. Moon, E. B. Kim, S. J. Hong, and H. S. Kim, “Structure and properties of ultrafine-grained CoCrFeMnNi high-entropy alloys produced by mechanical alloying and spark plasma sintering,” *J. Alloys Compd.*, vol. 698, pp. 591–604, 2017, doi: 10.1016/j.jallcom.2016.12.010.

[52] R. M. Pohan, B. Gwalani, J. Lee, T. Alam, J. Y. Hwang, H. J. Ryu, R. Banerjee, and S. H. Hong, “Microstructures and mechanical properties of mechanically alloyed and spark plasma sintered Al0.3CoCrFeMnNi high entropy alloy,” *Mater. Chem. Phys.*, vol. 210, pp. 62–70, 2018, doi: 10.1016/j.matchemphys.2017.09.013.

[53] W. R. Wang, W. L. Wang, S. C. Wang, Y. C. Tsai, C. H. Lai, and J. W. Yeh, “Effects of Al addition on the microstructure and mechanical property of Al xCoCrFeNi high-entropy alloys,” *Intermetallics*, vol. 26, pp. 44–51, 2012, doi: 10.1016/j.intermet.2012.03.005.

[54] C. C. Tung, J. W. Yeh, T. tsung Shun, S. K. Chen, Y. S. Huang, and H. C. Chen, “On the elemental effect of AlCoCrCuFeNi high-entropy alloy system,” *Mater. Lett.*, vol. 61, no. 1, pp. 1–5, 2007, doi: 10.1016/j.matlet.2006.03.140.

[55] H. R. Sistla, J. W. Newkirk, and F. Frank Liou, “Effect of Al/Ni ratio, heat treatment on phase transformations and microstructure of AlxFeCoCrNi2-x (x=0.3, 1) high entropy alloys,” *Mater. Des.*, vol. 81, pp. 113–121, 2015, doi: 10.1016/j.matdes.2015.05.027.

[56] J. T. Liang, K. C. Cheng, Y. C. Chen, S. M. Chiu, C. Chiu, J. W. Lee, and S. H. Chen, “Comparisons of plasma-sprayed and sputtering Al0.5CoCrFeNi2 high-entropy alloy coatings,” *Surf. Coatings Technol.*, vol. 403, no. September, p. 126411, 2020, doi: 10.1016/j.surfcoat.2020.126411.

[57] H. Shingu, “Mechanical alloying,” *J. Japan Inst. Light Met.*, vol. 40, no. 11, pp. 850–855, 1990, doi: 10.2464/jilm.40.850.

[58] C. Suryanarayana, E. Ivanov, and V. V. Boldyrev, “The science and technology of mechanical alloying,” *Mater. Sci. Eng. A*, vol. 304–306, no. 1–2, pp. 151–158, 2001, doi: 10.1016/S0921-5093(00)01465-9.

[59] L. V. M. Antony and R. G. Reddy, “Processes for production of high-purity metal powders,” *Jom*, vol. 55, no. 3, pp. 14–18, 2003, doi: 10.1007/s11837-003-0153-4.

[60] A. S. Baskoro, S. Supriadi, and Dharmanto, “Review on Plasma Atomizer Technology for Metal Powder,” *MATEC Web Conf.*, vol. 269, p. 05004, 2019, doi: 10.1051/matecconf/201926905004.

[61] S. D. Al-Shobaki, “Pinning Effect of Pores on Grain Growth in Sintered Steel,” *Jordan J. Mech. Ind. Eng.*, vol. 5, no. 3, pp. 267–272, 2007.

[62] H. C. Pavanati, A. M. Maliska, A. N. Klein, and J. L. R. Muzart, “Comparative study of porosity and pores morphology of unalloyed iron sintered in furnace and plasma reactor,” *Mater. Res.*, vol. 10, no. 1, pp. 87–93, 2007, doi: 10.1590/S1516-14392007000100019.

[63] W. Y. Shih, W.-H. Shih, and I. A. Aksay, “Elimination of an isolated pore: Effect of grain size,” *J. Mater. Res.*, vol. 10, no. 4, pp. 1000–1015, Apr. 1995, doi: 10.1557/JMR.1995.1000.

[64] S.-J. L. Kang, *Sintering: densification, grain growth and microstructure*. Elsevier, 2004.

[65] T. O. Saetre, N. Ryum, and O. Hunderi, “The effect of grain boundary edges on grain growth and grain growth stagnation,” *Mater. Sci. Eng. A*, vol. 108, no. C, pp. 33–36, 1989, doi: 10.1016/0921-5093(89)90403-6.

[66] N. Kurgan, “Effect of porosity and density on the mechanical and microstructural properties of sintered 316L stainless steel implant materials,” *Mater. Des.*, vol. 55, pp. 235–241, 2014, doi: 10.1016/j.matdes.2013.09.058.

[67] B. Dubrujeaud, M. Vardavoulias, and M. Jeandin, “The role of porosity in the dry sliding wear of a sintered ferrous alloy,” *Wear*, vol. 174, no. 1–2, pp. 155–161, 1994, doi: 10.1016/0043-1648(94)90097-3.

[68] Z. Tan, L. Wang, Y. Xue, P. Zhang, T. Cao, and X. Cheng, “High-entropy alloy particle reinforced Al-based amorphous alloy composite with ultrahigh strength prepared by spark plasma sintering,” *Mater. Des.*, vol. 109, pp. 219–226, 2016, doi: 10.1016/j.matdes.2016.07.086.

[69] Z. Yuan, W. Tian, F. Li, Q. Fu, X. Wang, W. Qian, and W. An, “Effect of heat treatment on the interface of high-entropy alloy particles reinforced aluminum matrix composites,” *J. Alloys Compd.*, vol. 822, p. 153658, 2020, doi: 10.1016/j.jallcom.2020.153658.

[70] M. A. Asadabad and M. J. Eskandari, “Electron Diffraction,” *Mod. Electron Microsc. Phys. Life Sci.*, no. March, 2016, doi: 10.5772/61781.

[71] N. V. Kazantseva, V. P. Pilyugin, S. E. Danilov, and V. Y. Kolosov, “Effect of severe plastic deformation on the structure and crystal-lattice distortions in the Ni3(Al,X) (X = Ti, Nb) intermetallic compound,” *Phys. Met. Metallogr.*, vol. 116, no. 5, pp. 501–508, 2015, doi: 10.1134/S0031918X15050075.

Publication:

1. Analyzing the Phase evolution, Microstructure and Wear Response of Spark Plasma Sintered $Al_{0.5}CoCrFeNi_2$ High Entropy Superalloy.
   Journal: Advanced Engineering Materials
   DOI: 10.1002/adem.202201523

VITA

ABHISHEK TIKAR

Candidate for the Degree of

Master of Science

Thesis: PHASE EVOLUTION, MICROSTRUCTURE AND WEAR BEHAVIOR OF

$Al_{0.5}CoCrFeNi_2$ HIGH ENTROPY SUPERALLOY AND Al/$Al_{0.5}CoCrFeNi_2$

COMPOSITES PROCESSED USING SPARK PLASMA SINTERING

Major Field: Mechanical and Aerospace Engineering

Biographical:

Education:

Completed the requirements for the Master of Science in your major at Oklahoma State University, Stillwater, Oklahoma in May, 2023.

Completed the requirements for the Bachelor of Technology in Metallurgical Engineering at College of Engineering, Pune, India in May, 2018.

Experience:

Graduate research and teaching assistant in Mechanical and Aerospace Engineering department at Oklahoma State University.